Journal of Sound and Vibration 329 (2010) 3565–3586

Contents lists available at ScienceDirect

Journal of Sound and Vibration

journal homepage: www.elsevier.com/locate/jsvi

Dynamic analysis of horizontal axis wind turbine by thin-walled beam theory

Jianhong Wang [a,*], Datong Qin [a], Teik C. Lim [b]

[a] State Key Lab of Mechanical Transmission, Chongqing University, Chongqing 400044, PR China
[b] Department of Mechanical Engineering, University of Cincinnati, 598 Rhodes Hall, P.O. Box 210072, Cincinnati, OH 45221, USA

ARTICLE INFO

Article history:
Received 2 October 2009
Received in revised form
30 January 2010
Accepted 6 March 2010
Handling Editor: H. Ouyang
Available online 7 April 2010

ABSTRACT

A mixed flexible-rigid multi-body mathematical model is applied to predict the dynamic performance of a wind turbine system. Since the tower and rotor are both flexible thin-walled structures, a consistent expression for their deformations is applied, which employs a successive series of transformations to locate any point on the blade and tower relative to an inertial coordinate system. The kinetic and potential energy terms of each flexible body and rigid body are derived for use in the Lagrange approach to formulate the wind turbine system's governing equation. The mode shapes are then obtained from the free vibration solution, while the distributions of dynamic stress and displacement of the tower and rotor are computed from the forced vibration response analysis. Using this dynamic model, the influence of the tower's stiffness on the blade tip deformation is studied. From the analysis, it is evident that the proposed model not only inherits the simplicity of the traditional 1-D beam element, but also able to provide detailed information about the tower and rotor response due to the incorporation of the flexible thin-walled beam theory.

1. Introduction

Wind turbine technology, while gaining more popularity in recent years, is also experiencing many critical challenges related to loading and size increase, which can hamper further advancement and stifle its expansion. To deal with this impediment, engineers have attempted to continuously adapt the fundamental wind turbine technology and design. This evolution is discussed by Quarton in a publication [1] that surveyed the design and analysis of wind turbine during the last two decades preceding 1998. The paper reviewed the dominant factors driving the design process and evaluated the state-of-the-art capabilities. In addition, Quarton analyzed the uncertainty areas and likely future developments of wind turbine design.

There are a number of investigations [2–7] aimed mainly at modeling the dynamic performance of the blade. Even though numerous mathematical models were applied, the finite element model is by far the most widely used one. These studies investigated blade deformation, natural modes, effect of turbulence and other relevant dynamic response. There are also other investigations [8–11] focused primarily on the tower's dynamic behavior and various aspects of structural design including optimization of tower shape to improve dynamic performance.

In spite of the above-mentioned work and other studies on wind turbine dynamics, there are surprisingly very few mathematical modeling efforts that consider the flexibilities of the rotor and tower as well as their dynamic coupling. In a

* Corresponding author.
E-mail address: jhwang@cqu.edu.cn (J. Wang).

0022-460X/$ - see front matter © 2010 Elsevier Ltd. All rights reserved.
doi:10.1016/j.jsv.2010.03.011

Nomenclature

A	area of cross section
c_c	the chord length of the cross section
C_L, C_D	the lift and drag coefficients
d_x, d_y, d_z	the components of the rigid translation of $\mathbf{d}$
D, d	the external and internal diameters of the tower
H	longitudinal length of the tower
$\mathbf{H}$, $\mathbf{H}_1$, $\mathbf{H}_2$	elemental shape function vector and its 1st and 2nd derivatives coefficient vector
i_x, i_y, i_z	the components of unit vector $\mathbf{i}$
I	second or higher order moment of the area
J_r	rotor's moment of inertia
K	kinetic energy
$\mathbf{K}$	stiffness matrix of the wind turbine
L	distance from the tower axis to the rotor's rotation plane
L_a	the Lagrangian function
m_n	total nacelle mass
$\mathbf{M}(w'_{t0})$	mass matrix of the wind turbine
N	number of blades
N_b, N_t	number of finite element on each blade and number of finite element on the tower
$\mathbf{q}$, $\mathbf{q}'$	the deformation state vector and corresponding derivative
$\mathbf{Q}(w'_{t0})$	external force vector of the wind turbine
R	distance form cross section to the rotor coordinate system $x_r y_r z_r$
S	first moment of the area
ΔS	displacement along circumference of point p
$\mathbf{T}_{br}$	transformation matrix from the cross section coordinate system $x_b y_b z_b$ to the rotor coordinate system $x_r y_r z_r$
$\mathbf{T}_f$	transformation matrix of the flexible body deformation
$\mathbf{T}_{n0}$	transformation matrix from the nacelle coordinate system $x_n y_n z_n$ to the wind turbine inertial coordinate system $x_0 y_0 z_0$
$\mathbf{T}_r$	rigid transformation matrix
$\mathbf{T}_{rn}$	transformation matrix from the rotor coordinate system $x_r y_r z_r$ to the nacelle coordinate system $x_n y_n z_n$
u, v, w	beam's deformation in x_1, y_1 and z_1 axes
U	potential energy
V_∞	the absolute wind velocity
W_a	virtual work due to the aerodynamic load
W_c	virtual work due to centrifugal force
W_g	virtual work due to gravity
W_t	virtual work of the moment produced by the aerodynamic load
w'_{t0}	tower's most top bending slope
x_g, y_g, z_g	the nacelle's gravity center coordinates

Greek symbols

α	blade's twist angle
β	blade's attack angle
γ	blade's pitch angle
ε_{bxx}, ε_{bxy}, ε_{bxz}	blade's linear strains
ε_{txx}, ε_{txz}	tower's linear strains
ε_{xs}	thin-walled beam's shear strain
θ	the rigid rotation angle of the cross section
κ	warping function
λ	the tangential angle at point p
ξ, η	coordinates of point p relative to the cross section coordinate system
σ, τ	axial stress and shear stress
ϕ	flexible body rotation
φ	rigid rotation angle
ω	rotor angular velocity

Subscript

0	the inertial system
b	the blade
n	the nacelle
r	the rotor
t	the tower

Superscript

e	the element

Special functions

$\otimes$	Kronecker product

rare case, Garrad and Quarton [12] used a symbolic computing tool to derive the coupled rotor-tower system equations of motion and then applied those equations to examine the stability of a simple example. In another study, Stol, Balas and Bir [13] built a two-bladed wind turbine structural model with seven degrees-of-freedom that includes tower fore-aft bending, tower lateral bending, tower twist, nacelle yaw, hub teeter and flapwise bending of each blade. The Floquet theory was then used to extract the modal parameters. In this analysis, the centrifugal and gyroscopic effects were shown to have a significant effect on wind turbine modes, especially at high rotor speed.

Fairly recently, Larsen and Nielsen [14] studied the nonlinear parametric instability of a wind turbine wings using a two degrees-of-freedom model. Their model was used to analyze the blade vibrations in the flapwise and edgewise directions. They computed the combination of amplitudes and frequencies that would lead to instability of the wind turbine.

As the size and capacity of wind turbine increase, structural flexibility becomes a critical concern and earlier lumped parameter models may be inadequate. In a study to address this concern, Ahlstrom [15] applied a commercial finite

element software package to develop a flexible structural dynamic model of a wind turbine. The model was employed to investigate the system dynamic response due to wind load on the blades for a range of blade slenderness ratios and wind conditions. The analysis concluded that large blade deflections have major influence on the power production and structural loads.

In another pair of finite element studies, Lee, Hodges and Patil [16,17] constructed a wind turbine model comprising of both rigid body and flexible body subsystems. The model applied the traditional 1-D finite element to represent the flexibility of the rotor and tower while the rest of the wind turbine components are assume to be rigid bodies. The system's governing equations were obtained by coupling the rigid body equation of motion to the linearized flexible body model of the tower–rotor subsystem. The resultant system equations of motion were treated using the Floquet theory to extract the wind turbine dynamic characteristics. Since this model was mainly developed for wind turbine control study, which already requires high computational efficiency, the structure model was made quite coarse from the viewpoint of structural dynamics.

All of the prior research studies on the dynamic interaction between the tower and rotor as discussed above adopt the 1-D beam finite element representation to model the deformed state of both the rotor and the tower. The reason is because it is simple and requires less computing effort. However, this modeling concept has a serious disadvantage if the displacements and stresses on the skin panel of the tower and blade are needed. In order to be able to calculate the panel displacement and stress response, one possible approach is to discretize the skin panel structure using 2-D shell elements. However, the total degrees-of-freedom will certainly rise significantly, which will in turn increase the computational cost tremendously. Overcoming this computational limitation is the focus of present study, which will be described next.

This paper presents an analytical approach to address the limitations of previous wind turbine models in analyzing the complex dynamic response of tower–blade interactions. The proposed mathematical model that employs a mixed flexible-rigid multi-body formulation possesses the simplicity of the traditional 1-D beam finite element concept while at the same time yields detailed response information of the flexible tower and rotor structures. In the proposed approach, two matrix transformations are defined to relate the rotation and translation coordinates of the flexible elements to the rigid body motion. Also, a thin-walled structure theory is applied to obtain the displacement of any point in the tower and rotor. The formulation of the shape function of the 1-D beam finite element along with their first two derivatives with respect to beam's axial coordinates is presented. From the displacement equations, the kinetic and potential energy terms of both the rotor and the tower are derived. The virtual work needed for the derivation of the system equations of motion account for external loads such as aerodynamic and centrifugal forces on the blade and gravitational effect. The resultant system's governing equations are then derived using the Lagrange method. Free vibration analysis is performed to obtain the natural modes of the coupled tower–rotor system. In addition, the dynamic displacement field and stress distribution in the tower and rotor subject to constant wind speed are computed from the forced response analysis. The effect of tower stiffness on blade tip gross displacement is examined. Finally, to avoid unnecessary modeling complications, the materials of the blade and tower are assumed to be isotropic and homogeneous, and all flexible deformations are considered to be relatively small.

2. Wind turbine analytical model

2.1. Coordinate transformations

Consider a thin-walled beam as illustrated in Fig. 1. The beam geometry is defined relative to the Cartesian coordinate system *oxyz* with its longitudinal *x*-axis running through the shear center of cross section. An arbitrary cross section represented by the solid line shown with R as the length distance along the x-axis and rigid rotation angle θ is defined by the coordinate system $o_1x_1y_1z_1$ of the undeformed state. The corresponding deformed position, shown as dashed line, after undergoing displacements u, v and w along the axes of x_1, y_1 and z_1 is represented by $\tau\chi\zeta\eta$. During deformation, the cross section also experiences a rotation ϕ with respect to its longitudinal x_1-axis. The angle ϕ denotes the flexible body rotation. The first-order transformation matrix of the flexible body deformation between $o_1x_1y_1z_1$ and $\tau\chi\xi\eta$ is given by [18,19]

$$\mathbf{T}_f(u,v,w,\phi)=\begin{bmatrix} 1 & v' & w' & u \\ -v' & 1 & \phi & v \\ -w' & \phi & 1 & w \\ 0 & 0 & 0 & 1 \end{bmatrix} \tag{1}$$

where $(\ )'=\mathrm{d}(\ )/\mathrm{d}x$. Here, the translational components in Eq. (1) are set to zero due to the beam small deformation assumption.

The companion transformation matrix for rigid body motion, which is critical to the proposed formulation, is considered next. When a coordinate system of a rigid body rotates about a unit vector $\mathbf{i}(i_x,i_y,i_z)$ with an angle φ and then

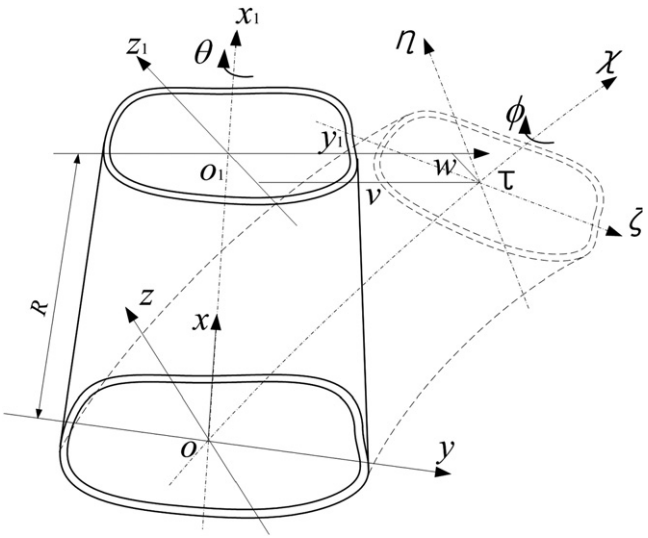

Fig. 1. Undeformed (solid line) and deformed positions of a thin-walled beam structure.

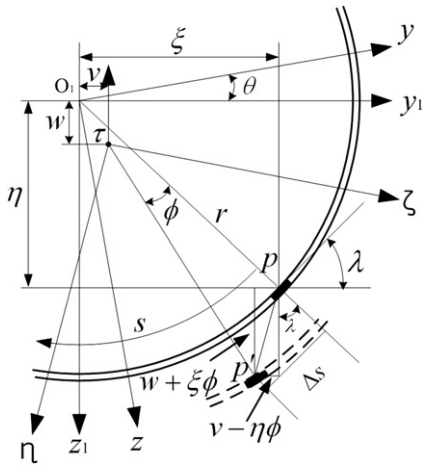

Fig. 2. Kinematics of a cross section of the thin-walled beam structure.

followed by a translation $\mathbf{d}(d_x,d_y,d_z)$, the transformation matrix $\mathbf{T}_r$ describing this pair of motion can be defined as [20]

$$\mathbf{T}_r(\mathbf{i}(i_x,i_y,i_z),\varphi,\mathbf{d}(d_x,d_y,d_z)) = \begin{bmatrix} i_x^2(1-\cos\varphi)+\cos\varphi & i_xi_y(1-\cos\varphi)-i_z\sin\varphi & i_xi_z(1-\cos\varphi)+i_y\sin\varphi & d_x \\ i_xi_y(1-\cos\varphi)+i_z\sin\varphi & i_y^2(1-\cos\varphi)+\cos\varphi & i_yi_z(1-\cos\varphi)-i_x\sin\varphi & d_y \\ i_xi_z(1-\cos\varphi)-i_y\sin\varphi & i_yi_z(1-\cos\varphi)+i_x\sin\varphi & i_z^2(1-\cos\varphi)+\cos\varphi & d_z \\ 0 & 0 & 0 & 1 \end{bmatrix} \quad (2)$$

where i_x, i_y and i_z are the components of unit vector **i**, while d_x, d_y and d_z are the components of translation vector **d**.

2.2. Kinematics of thin-walled beam cross section

A segment of the cross section of the thin-walled beam structure is illustrated in Fig. 2. In this schematic, a point p on the wall, which is defined by the distance s along the circumference, is displaced by the circumferential displacement Δs to a new point p'. At point p, the tangential angle with respect to y_1-axis is denoted by λ. During the deformation, the cross sectional shape of the thin-walled structure is assumed to be unaltered. This means that any cross section normal to the longitudinal axis remains unchanged. Therefore, the displacements of the cross section, namely v and w along the axes of y_1 and z_1, respectively, are only functions of x. Furthermore; the thin-walled structure is flexible enough that the effect of the shear strain ε_{xs} on the final deformation is small enough to be neglected.

Based on above conditions, the following relation can be obtained for the shear strain:

$$\varepsilon_{xs} = \frac{\partial u}{\partial s} + \frac{\partial \Delta s}{\partial x} \approx 0 \tag{3}$$

The displacement of point p along the circumference is given by

$$\Delta s = (w + \xi\phi)\sin\lambda + (v - \eta\phi)\cos\lambda = w\sin\lambda + v\cos\lambda + \kappa\phi \tag{4}$$

where ξ and η are the coordinates of position p relative to the cross section coordinate system defined by the axes of y_1 and z_1. Substituting Δs from Eq. (4) into Eq. (3) yields

$$\frac{\partial u}{\partial s} = -\frac{\partial \Delta s}{\partial x} = -\frac{\mathrm{d}v}{\mathrm{d}x}\cos\lambda - \frac{\mathrm{d}w}{\mathrm{d}x}\sin\lambda + \frac{\mathrm{d}\phi}{\mathrm{d}x}\kappa \tag{5}$$

where $\kappa = c\xi\eta$ is the warping function, c is a coefficient and

$$\sin\lambda = \mathrm{d}\eta/\mathrm{d}s, \quad \cos\lambda = \mathrm{d}\xi/\mathrm{d}s \tag{6a,b}$$

Further substitution of Eq. (6) into Eq. (5), multiplying through by ds and then integrating will lead to the displacement of point p' as

$$\begin{aligned}
\Delta\mathbf{p}(u,v,w,\phi,\theta) &= \begin{Bmatrix} \Delta x \\ \Delta y \\ \Delta z \end{Bmatrix} = \begin{Bmatrix} u \\ v \\ w \end{Bmatrix} + \begin{bmatrix} 1 & 0 & 0 \\ 0 & \cos\theta & -\sin\theta \\ 0 & \sin\theta & \cos\theta \end{bmatrix} \begin{Bmatrix} -\xi v' - \eta w' - c\xi\eta\phi' \\ -\eta\phi \\ \xi\phi \\ 0 \end{Bmatrix} \\
&= \begin{bmatrix} 1 & 0 & 0 & 0 & 0 \\ 0 & 1 & 0 & -\eta\cos\theta - \xi\sin\theta & \xi\cos\theta - \eta\sin\theta \\ 0 & 0 & 1 & -\eta\sin\theta + \xi\cos\theta & \xi\sin\theta + \eta\cos\theta \\ 0 & 0 & 0 & 0 & 1 \end{bmatrix} \begin{Bmatrix} u \\ v \\ w \\ \phi \\ 1 \end{Bmatrix} + \begin{bmatrix} 0 & -\xi & -\eta & -c\xi\eta & 0 \\ 0 & 0 & 0 & 0 & 0 \\ 0 & 0 & 0 & 0 & 0 \\ 0 & 0 & 0 & 0 & 0 \end{bmatrix} \begin{Bmatrix} u' \\ v' \\ w' \\ \phi' \\ 0 \end{Bmatrix} \\
&= \mathbf{D}_1 \begin{Bmatrix} \mathbf{q} \\ 1 \end{Bmatrix} + \mathbf{D}_2 \begin{Bmatrix} \mathbf{q}' \\ 0 \end{Bmatrix}
\end{aligned} \tag{7}$$

where $\mathbf{q} = \{u \;\; v \;\; w \;\; \phi\}^{\mathrm{T}}$ and $\mathbf{q}' = \{u' \;\; v' \;\; w' \;\; \phi'\}^{\mathrm{T}}$.

2.3. Thin-walled beam element

In the thin-walled beam element shown in Fig. 3, the x-axis runs through the shear center of the element, and the axes of y and z are arbitrarily oriented in a plane orthogonal to the x-axis to define a cross section. There are three nodes, labeled as $i-1$, i and $i+1$, which are used to determine the behavior of the element. The nodal displacements are given by u, v and w along the axes of x, y and z, respectively. A local longitudinal coordinate r is a directed line segment from node i to node $i+1$. The deformation pattern of any point along the x-axis can be determined directly by [21]

$$\mathbf{q} = \sum_{i=1}^{3} h_i \mathbf{q}_i^e = \mathbf{H}\mathbf{q}^e \tag{8}$$

where superscript e denotes finite element, and h is the elemental shape function for thin-walled beam given by

$$h_1 = \tfrac{1}{2}r(r-1), \quad h_2 = 1 - r^2, \quad h_3 = \tfrac{1}{2}r(r+1) \tag{9a–c}$$

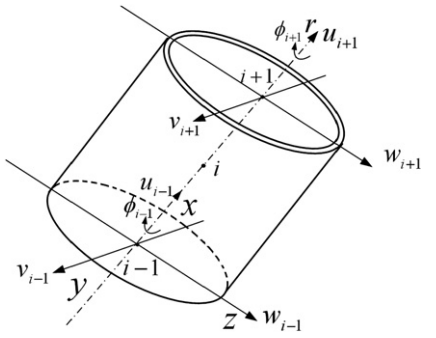

Fig. 3. A thin-walled beam element.

Based on the above deformation patterns and the assumption that node i is the midpoint of the element along the longitudinal axis, the first derivative of Eq. (8) with respect to x turns out to be

$$\mathbf{q}' = \frac{\partial \mathbf{q}}{\partial r}\frac{\partial r}{\partial x} = \frac{\partial \mathbf{q}}{\partial r}\Big/\frac{\partial x}{\partial r} = \sum_{i=1}^{3}\left(\frac{\partial h_i}{\partial r}\Big/\sum_{j=1}^{3}\frac{\partial h_j}{\partial r}x_j\right)\mathbf{q}_i^e = \sum_{i=1}^{3}\left(\frac{2}{l^e}\frac{\partial h_i}{\partial r}\right)\mathbf{q}_i^e = \sum_{i=1}^{3}k_i^1\mathbf{q}_i^e = \mathbf{H}_1\mathbf{q}^e \tag{10}$$

where l^e is the thin-walled beam element length. Similarly, the second derivative is of the form,

$$\mathbf{q}'' = \frac{\partial^2 \mathbf{q}}{\partial x^2} = \sum_{i=1}^{3}\left(\frac{2}{l^e}\right)^2\frac{\partial^2 h_i}{\partial r^2}\mathbf{q}_i^e = \sum_{i=1}^{3}k_i^2\mathbf{q}_i^e = \mathbf{H}_2\mathbf{q}^e \tag{11}$$

2.4. Rotor modeling

To model the dynamics of the rotor, a set of coordinate systems for the wind turbine as shown in Fig. 4 are employed. The inertial coordinate system of the wind turbine is denoted by $x_0y_0z_0$ where the x_0 runs vertically through the tower axis and z_0 points in the wind direction. The nacelle and all its internal components are represented by the coordinate system $x_ny_nz_n$ in which x_n points forward and z_n points upward. The rotor coordinate system with origin at the center of its shaft is $x_ry_rz_r$, while $x_by_bz_b$ is the coordinate system at a cross section R distance from the origin of the rotor coordinate system along the blade axis.

Next, a set of coordinate transformations are defined as follows. The transformations from the local cross section coordinate system $x_by_bz_b$ to the rotor coordinate system $x_ry_rz_r$ involve a translation of magnitude R in the negative x_b direction, and followed by a pair of back-to-back 90° rotations about the y_b and z_b axes. The corresponding transformation matrix $\mathbf{T}_{br}$ between the cross section coordinate system and rotor coordinate system can be written as

$$\mathbf{T}_{br} = \mathbf{T}_r^{-1}(\mathbf{i}(0,0,1),\pi/2,\mathbf{d}(0,0,0))\cdot\mathbf{T}_r^{-1}(\mathbf{i}(0,1,0),\pi/2,\mathbf{d}(-R,0,0)) \tag{12}$$

The transformation from the rotor coordinate system to the nacelle coordinate system is actually quite simple since it involves a translation along the negative x_r direction of distance L. Hence, the transformation matrix $\mathbf{T}_{rn}$ between the rotor

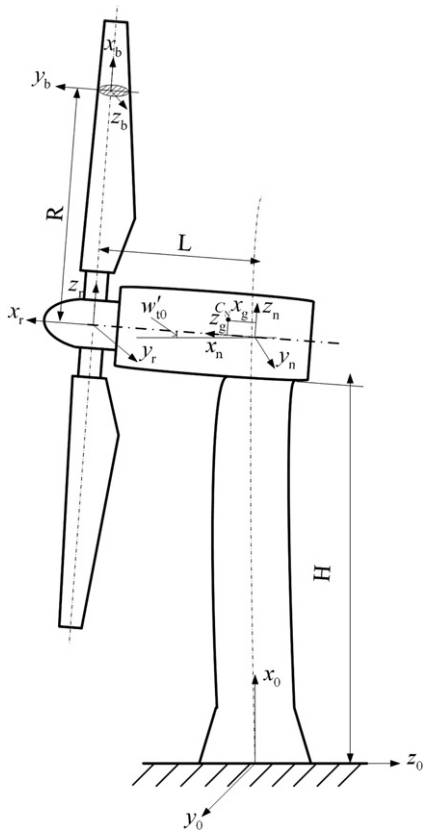

Fig. 4. The various coordinate systems applied in the wind turbine model.

and nacelle coordinate systems is

$$\mathbf{T}_{rn}=\mathbf{T}_r^{-1}(\mathbf{i}(0,0,0),0,\mathbf{d}(-L,0,0)) \tag{13}$$

Lastly, the transformation from the nacelle coordinate system to the wind turbine inertial coordinate system involves a downward translation of distance H followed by a minus 90° rotation about the y_n-axis. This transformation matrix $\mathbf{T}_{n0}$ is given by

$$\mathbf{T}_{n0}=\mathbf{T}_r^{-1}(\mathbf{i}(0,1,0),-\pi/2,\mathbf{d}(0,0,-H)) \tag{14}$$

2.4.1. Kinetic energy of rotor

Before proceeding further to derive the rotor kinetic energy term, the geometrical properties of the blade cross section are defined as follows:

$$A=\int_A \mathrm{d}A,\quad S_\xi=\int_A \eta\,\mathrm{d}A,\quad S_\eta=\int_A \xi\,\mathrm{d}A,\quad I_{\xi\xi}=\int_A \eta^2\,\mathrm{d}A,\quad I_{\eta\eta}=\int_A \xi^2\,\mathrm{d}A,\quad I_{\xi\eta}=\int_A \xi\eta\,\mathrm{d}A=\int_A \eta\xi\,\mathrm{d}A$$

$$I_{\xi\eta\eta}=\int_A \xi^2\eta\,\mathrm{d}A=\int_A \eta\xi^2\,\mathrm{d}A,\quad I_{\xi\xi\eta}=\int_A \xi\eta^2\,\mathrm{d}A=\int_A \eta^2\xi\,\mathrm{d}A,\quad I_{\xi\xi\xi}=\int_A \eta^3\,\mathrm{d}A,\quad I_{\eta\eta\eta}=\int_A \xi^3\,\mathrm{d}A \tag{15a–j}$$

where A is the area of the cross section, S is the first moment of the area and I is the second or higher order moment of the area. Then, by applying the previously defined successive transformations involving both translations and rotations, the position vector of an arbitrary point $\mathbf{p}$ on the blades can be expressed within the inertial coordinate system $x_0y_0z_0$ as

$$\mathbf{p}_b=\mathbf{T}_f(0,w_{t0},0)\cdot\mathbf{T}_{n0}\cdot\mathbf{T}_{rn}\cdot\mathbf{T}_{br}\cdot\Delta\mathbf{p}=\mathbf{T}_f\cdot\mathbf{T}_{n0}\cdot\mathbf{T}_{rn}\cdot\mathbf{T}_{br}\cdot\left(\mathbf{D}_1\begin{Bmatrix}\mathbf{q}_b\\1\end{Bmatrix}+\mathbf{D}_2\begin{Bmatrix}\mathbf{q}'_b\\0\end{Bmatrix}\right)=\mathbf{T}_f\cdot\left(\mathbf{B}_1\begin{Bmatrix}\mathbf{q}_b\\1\end{Bmatrix}+\mathbf{B}_2\begin{Bmatrix}\mathbf{q}'_b\\0\end{Bmatrix}\right) \tag{16}$$

where the subscript b associates the variable vector to the blade. Differentiating Eq. (16) with respect to time t gives the velocity of point $\mathbf{p}$ to be

$$\dot{\mathbf{p}}_b=\dot{\mathbf{T}}_f\cdot\left(\mathbf{B}_1\begin{Bmatrix}\mathbf{q}_b\\1\end{Bmatrix}+\mathbf{B}_2\begin{Bmatrix}\mathbf{q}'_b\\0\end{Bmatrix}\right)+\mathbf{T}_f\cdot\left(\mathbf{B}_1\begin{Bmatrix}\dot{\mathbf{q}}_b\\0\end{Bmatrix}+\mathbf{B}_2\begin{Bmatrix}\dot{\mathbf{q}}'_b\\0\end{Bmatrix}\right) \tag{17}$$

Having the velocity expression above enables one to formulate the kinetic energy of the blade as

$$K_b=\int_m \dot{\mathbf{p}}_b^{\mathrm{T}}\dot{\mathbf{p}}_b\,\mathrm{d}m=K_{qq}+K_{ww}+2K_{wq} \tag{18a}$$

$$\begin{aligned}K_{qq}=&\int[\dot{\mathbf{q}}_b^{\mathrm{T}}(\mathbf{T}_f\mathbf{B}_1)^{\mathrm{T}}(\mathbf{T}_f\mathbf{B}_1)\dot{\mathbf{q}}_b+\dot{\mathbf{q}}_b'^{\mathrm{T}}(\mathbf{T}_f\mathbf{B}_2)^{\mathrm{T}}(\mathbf{T}_f\mathbf{B}_2)\dot{\mathbf{q}}'_b+2\cdot\dot{\mathbf{q}}_b^{\mathrm{T}}(\mathbf{T}_f\mathbf{B}_1)^{\mathrm{T}}(\mathbf{T}_f\mathbf{B}_2)\dot{\mathbf{q}}'_b]\,\mathrm{d}m_b\\=&\sum_{j=1}^{N}\left(\begin{array}{l}\dfrac{1}{2}\rho_b\displaystyle\sum_{i=1}^{N_b}l_{ji}^e\mathbf{q}_{bji}^{e\mathrm{T}}\left(\int_{-1}^{1}\mathbf{H}^{\mathrm{T}}\mathbf{H}\otimes\begin{bmatrix}(1+w_{t0}'^2)A_{ji}&0&0&0\\&(1+w_{t0}'^2)A_{ji}&0&-(1+w_{t0}'^2)(S_{\eta ji}\sin\theta_{ji}+S_{\xi ji}\cos\theta_{ji})\\Sym.&&A_{ji}&S_{\eta ji}\cos\theta_{ji}-S_{\xi ji}\sin\theta_{ji}\\&&&I_{\xi\xi ji}[(1+w_{t0}'^2)\cos^2\theta_{ji}+\sin^2\theta_{ji}]+I_{\eta\eta ji}[(1+w_{t0}'^2)\sin^2\theta_{ji}+\cos^2\theta_{ji}]+I_{\xi\eta ji}w_{t0}'^2\sin2\theta_{ji}\end{bmatrix}\mathrm{d}r\right)\mathbf{q}_{bji}^e\\+\dfrac{1}{2}\rho_b\displaystyle\sum_{i=1}^{N_b}l_{ji}^e\mathbf{q}_{bji}^{e\mathrm{T}}\left(\int_{-1}^{1}\mathbf{H}_1^{\mathrm{T}}\mathbf{H}_1\otimes\begin{bmatrix}0&0&0&0\\&(1+w_{t0}'^2)I_{\eta\eta ji}&(1-w_{t0}'^2)I_{\xi\eta ji}&(1-w_{t0}'^2)cI_{\xi\eta\eta ji}\\Sym.&&(1+w_{t0}'^2)I_{\xi\xi ji}&(1+w_{t0}'^2)cI_{\xi\xi\eta ji}\\&&&(1+w_{t0}'^2)c^2I_{\xi\eta ji}^2\end{bmatrix}\mathrm{d}r\right)\mathbf{q}_{bji}^e\\+\dfrac{1}{2}\rho_b\displaystyle\sum_{i=1}^{N_b}l_{ji}^e\mathbf{q}_{bji}^{e\mathrm{T}}\left(\int_{-1}^{1}\mathbf{H}_1^{\mathrm{T}}\mathbf{H}\otimes\begin{bmatrix}0&-(1-w_{t0}'^2)S_{\eta ji}&-(1+w_{t0}'^2)S_{\xi ji}&-(1+w_{t0}'^2)cI_{\xi\eta ji}\\0&2w_{t0}'^2S_{\eta ji}&0&(1-w_{t0}'^2)cI_{\xi\eta\eta ji}\\0&0&0&(1+w_{t0}'^2)cI_{\xi\xi\eta ji}\\0&2w_{t0}'(I_{\xi\eta ji}\cos\theta_{ji}+I_{\eta\eta ji}\sin\theta_{ji})&0&(1+w_{t0}'^2)c^2I_{\xi\eta ji}^2\end{bmatrix}\mathrm{d}r\right)\mathbf{q}_{bji}^e\end{array}\right)\end{aligned} \tag{18b}$$

$$K_{ww}=\int\dot{\mathbf{T}}_f^{\mathrm{T}}\cdot\left(\mathbf{B}_1\begin{Bmatrix}\mathbf{q}_b\\1\end{Bmatrix}+\mathbf{B}_2\begin{Bmatrix}\mathbf{q}'_b\\0\end{Bmatrix}\right)^{\mathrm{T}}\cdot\left(\mathbf{B}_1\begin{Bmatrix}\mathbf{q}_b\\1\end{Bmatrix}+\mathbf{B}_2\begin{Bmatrix}\mathbf{q}'_b\\0\end{Bmatrix}_b\right)\cdot\dot{\mathbf{T}}_f\,\mathrm{d}m_b\approx\dot{w}_{t0}'^2\rho_bJ_r \tag{18c}$$

$$\begin{aligned}K_{wq}=&\int\left(\mathbf{B}_1\begin{Bmatrix}\mathbf{q}_b\\1\end{Bmatrix}+\mathbf{B}_2\begin{Bmatrix}\mathbf{q}'_b\\0\end{Bmatrix}\right)^{\mathrm{T}}\dot{\mathbf{T}}_f^{\mathrm{T}}\cdot\mathbf{T}_f\cdot\left(\mathbf{B}_1\begin{Bmatrix}\mathbf{q}_b\\1\end{Bmatrix}+\mathbf{B}_2\begin{Bmatrix}\mathbf{q}'_b\\0\end{Bmatrix}\right)\mathrm{d}m_b\\\approx&\sum_{j=1}^{N}\left(\frac{1}{2}\dot{w}'_{t0}\sum_{i=1}^{N_b}l_{ji}^e\rho_b\left(\int_{-1}^{1}\mathbf{H}\otimes\begin{bmatrix}-LA_{ji}\\(R_i+H)A_{ji}\\0\\(R_i+H)(S_{\xi ji}\cos\theta_{ji}+S_{\eta ji}\sin\theta_{ji})\end{bmatrix}^{\mathrm{T}}\right)\mathrm{d}r\dot{\mathbf{q}}_{bji}^e\right)\end{aligned} \tag{18d}$$

where the symbol $\otimes$ denotes Kronecker product, N is the number of blade and N_b is the number of finite element on each blade.

2.4.2. Potential energy of rotor

Neglecting rigid body motion, the blade deformation relative to the inertial coordinate system can be written as

$$\begin{Bmatrix}\Delta x_b\\ \Delta y_b\\ \Delta z_b\end{Bmatrix}=\begin{bmatrix}1 & w'_{t0} & 0 & -w'_{t0}(\eta\cos\theta+\xi\sin\theta)\\ 0 & 0 & -1 & \eta\sin\theta-\xi\cos\theta\\ -w'_{t0} & 1 & 0 & -\eta\cos\theta-\xi\sin\theta\end{bmatrix}\begin{Bmatrix}u\\ v\\ w\\ \phi\end{Bmatrix}+\begin{bmatrix}0 & -\xi & -\eta & -c\xi\eta\\ 0 & 0 & 0 & 0\\ 0 & w'_{t0}\xi & w'_{t0}\eta & w'_{t0}c\xi\eta\end{bmatrix}\begin{Bmatrix}u'\\ v'\\ w'\\ \phi'\end{Bmatrix}$$
$$=\begin{Bmatrix}\mathbf{S}_{11}\\ \mathbf{S}_{12}\\ \mathbf{S}_{13}\end{Bmatrix}\mathbf{q}_b+\begin{Bmatrix}\mathbf{S}_{21}\\ \mathbf{S}_{22}\\ \mathbf{S}_{23}\end{Bmatrix}\mathbf{q}'_b \tag{19a}$$

Assuming small deformation, the linear strain theory can be developed in the following manner:

$$\varepsilon_{bxx}=\frac{\partial\Delta x_b}{\partial x}=\mathbf{S}_{11}\mathbf{q}'_b+\mathbf{S}_{21}\mathbf{q}''_b \tag{19b}$$

$$\varepsilon_{bxy}=\frac{\partial\Delta x_b}{\partial\xi}+\frac{\partial\Delta y_b}{\partial x}=\frac{\partial\mathbf{S}_{11}}{\partial\xi}\mathbf{q}_b+\left(\frac{\partial\mathbf{S}_{21}}{\partial\xi}+\mathbf{S}_{12}\right)\mathbf{q}'_b \tag{19c}$$

$$\varepsilon_{bxz}=\frac{\partial\Delta x_b}{\partial\eta}+\frac{\partial\Delta z_b}{\partial x}=\frac{\partial\mathbf{S}_{11}}{\partial\eta}\mathbf{q}_b+\left(\frac{\partial\mathbf{S}_{21}}{\partial\eta}+\mathbf{S}_{13}\right)\mathbf{q}'_b+\mathbf{S}_{23}\mathbf{q}''_b \tag{19d}$$

Using Eqs. (19a–d), the potential energy of the blade can be formulated as

$$\begin{aligned}U_b=&\int_V(E_b\varepsilon_{bxx}^{\mathrm{T}}\varepsilon_{bxx}+G_b\varepsilon_{bxy}^{\mathrm{T}}\varepsilon_{bxy}+G_b\varepsilon_{bxz}^{\mathrm{T}}\varepsilon_{bxz})\,\mathrm{d}V=\mathbf{q}_b^{\mathrm{T}}\int_V G_b\left(\frac{\partial\mathbf{S}_{11}^{\mathrm{T}}}{\partial\xi}\frac{\partial\mathbf{S}_{11}}{\partial\xi}+\frac{\partial\mathbf{S}_{11}^{\mathrm{T}}}{\partial\eta}\frac{\partial\mathbf{S}_{11}}{\partial\eta}\right)\mathrm{d}V\mathbf{q}_b\\
&+\mathbf{q}_b'^{\mathrm{T}}\int_V\left[E_b\mathbf{S}_{11}^{\mathrm{T}}\mathbf{S}_{11}+G_b\left(\frac{\partial\mathbf{S}_{21}}{\partial\xi}+\mathbf{S}_{12}\right)^{\mathrm{T}}\left(\frac{\partial\mathbf{S}_{21}}{\partial\xi}+\mathbf{S}_{12}\right)+G_b\left(\frac{\partial\mathbf{S}_{21}}{\partial\eta}+\mathbf{S}_{13}\right)^{\mathrm{T}}\left(\frac{\partial\mathbf{S}_{21}}{\partial\eta}+\mathbf{S}_{13}\right)\right]\mathrm{d}V\mathbf{q}'_b\\
&+\mathbf{q}_b''^{\mathrm{T}}\int_V[E_b\mathbf{S}_{21}^{\mathrm{T}}\mathbf{S}_{21}+G\mathbf{S}_{23}^{\mathrm{T}}\mathbf{S}_{23}]\mathrm{d}V\mathbf{q}''_b+\mathbf{q}_b^{\mathrm{T}}\int_V 2G\left[\frac{\partial\mathbf{S}_{11}^{\mathrm{T}}}{\partial\xi}\left(\frac{\partial\mathbf{S}_{21}}{\partial\xi}+\mathbf{S}_{12}\right)+\frac{\partial\mathbf{S}_{11}^{\mathrm{T}}}{\partial\eta}\left(\frac{\partial\mathbf{S}_{21}}{\partial\eta}+\mathbf{S}_{13}\right)\right]\mathrm{d}V\mathbf{q}'_b\\
&+\mathbf{q}_b^{\mathrm{T}}\int_V 2G_b\frac{\partial\mathbf{S}_{11}^{\mathrm{T}}}{\partial\eta}\mathbf{S}_{23}\,\mathrm{d}V\mathbf{q}''_b+\mathbf{q}_b'^{\mathrm{T}}\int_V 2\left[E_b\mathbf{S}_{11}^{\mathrm{T}}\mathbf{S}_{21}+G_b\left(\frac{\partial\mathbf{S}_{21}^{\mathrm{T}}}{\partial\eta}+\mathbf{S}_{13}^{\mathrm{T}}\right)\mathbf{S}_{23}\right]\mathrm{d}V\mathbf{q}''_b\\
=&\mathbf{q}_b^{\mathrm{T}}\mathbf{K}_{b1}\mathbf{q}_b+\mathbf{q}_b'^{\mathrm{T}}\mathbf{K}_{b2}\mathbf{q}'_b+\mathbf{q}_b''^{\mathrm{T}}\mathbf{K}_{b3}\mathbf{q}''_b+\mathbf{q}_b^{\mathrm{T}}\mathbf{K}_{b4}\mathbf{q}'_b+\mathbf{q}_b'^{\mathrm{T}}\mathbf{K}_{b5}\mathbf{q}''_b+\mathbf{q}_b'^{\mathrm{T}}\mathbf{K}_{b6}\mathbf{q}''_b=U_{b1}+U_{b2}+U_{b3}+U_{b4}+U_{b5}+U_{b6}\end{aligned} \tag{20}$$

where E_b and G_b are the blade elastic modulus and blade shear elastic modulus, respectively. Since the blade potential energy equation cannot be easily differentiated directly, it is necessary to utilize the thin-walled beam element defined in Eqs. (8)–(11) to formulate an alternate form of the potential energy,

$$U_{b1}=\sum_{j=1}^{N}\left(\frac{1}{2}G_b\sum_{i=1}^{N_b}l_{ji}^e\mathbf{q}_{bji}^{e\mathrm{T}}\left(\int_{-1}^{1}\mathbf{H}^{\mathrm{T}}\mathbf{H}\otimes\begin{bmatrix}0 & 0 & 0 & 0\\ & 0 & 0 & 0\\ Sym. & & 0 & 0\\ & & & w'^2_{t0}A_{ji}\end{bmatrix}\mathrm{d}r\right)\mathbf{q}_{bji}^e\right) \tag{21a}$$

$$U_{b2}=\sum_{j=1}^{N}\left(\begin{aligned}&\frac{1}{2}\sum_{i=1}^{N_b}l_{ji}^e\mathbf{q}_{bji}^{e\mathrm{T}}\Big(\int_{-1}^{1}\mathbf{H}_1^{\mathrm{T}}\mathbf{H}_1\otimes\Big(E_b\begin{bmatrix}A_{ji} & w'_{t0}A_{ji} & 0 & -w'_{t0}(S_{\xi ji}\cos\theta_{ji}+S_{\eta ji}\sin\theta_{ji})\\ & w'^2_{t0}A_{ji} & 0 & -w'^2_{t0}(S_{\xi ji}\cos\theta_{ji}+S_{\eta ji}\sin\theta_{ji})\\ Sym. & & 0 & 0\\ & & & w'^2_{t0}(I_{\xi\xi ji}\cos^2\theta_{ji}+I_{\eta\eta ji}\sin^2\theta_{ji}+I_{\xi\eta ji}\sin 2\theta_{ji})\end{bmatrix}\\
&+G_b\begin{bmatrix}0 & 0 & 0 & 0\\ & A_{ji} & A_{ji} & S_{\eta ji}\cos\theta_{ji}-S_{\xi ji}(\sin\theta_{ji}-c)\\ Sym. & & A_{ji} & S_{\eta ji}\cos\theta_{ji}-S_{\xi ji}(\sin\theta_{ji}-c)\\ & & & I_{\xi\xi ji}(\sin\theta_{ji}-c)^2+I_{\eta\eta ji}\cos^2\theta_{ji}-2I_{\xi\eta ji}\cos\theta_{ji}(\sin\theta_{ji}-c)\end{bmatrix}\\
&+G_b\begin{bmatrix}w'^2_{t0}A_{ji} & -w'_{t0}A_{ji} & w'_{t0}A_{ji} & w'_{t0}[S_{\xi ji}\cos\theta_{ji}+S_{\eta ji}(\sin\theta_{ji}+c)]\\ & A_{ji} & -A_{ji} & -[S_{\xi ji}\cos\theta_i+S_{\eta i}(\sin\theta_{ji}+c)]\\ Sym. & & A_{ji} & [S_{\xi ji}\cos\theta_i+S_{\eta i}(\sin\theta_{ji}+c)]\\ & & & I_{\eta\eta ji}(\sin\theta_{ji}+c)^2+I_{\xi\xi ji}\cos^2\theta_{ji}+2I_{\xi\eta ji}\cos\theta_{ji}(\sin\theta_{ji}+c)\end{bmatrix}\Big)\mathrm{d}r\Big)\mathbf{q}_{bji}^e\end{aligned}\right) \tag{21b}$$

$$U_{b3}=\sum_{j=1}^{N}\left(\frac{1}{2}\sum_{i=1}^{N_b}l_{ji}^{e}\mathbf{q}_{bji}^{eT}\Big(\int_{-1}^{1}\mathbf{H}_2^{T}\mathbf{H}_2\otimes\Big((E_b+w_{t0}'^2G_b)\begin{bmatrix}0&0&0&0\\ &I_{\eta\eta ji}&I_{\xi\eta ji}&cI_{\xi\eta\eta ji}\\ Sym.&&I_{\xi\xi ji}&cI_{\xi\xi\eta ji}\\ &&&c^2I_{\xi\eta ji}^2\end{bmatrix}\Big)\mathrm{d}r\Big)\mathbf{q}_{bji}^{e}\right) \tag{21c}$$

$$U_{b4}=\sum_{j=1}^{N}\left(\frac{1}{2}\sum_{i=1}^{N_b}l_{ji}^{e}\mathbf{q}_{bji}^{eT}\left(\int_{-1}^{1}\mathbf{H}_1^{T}\mathbf{H}\otimes\left(2G_b\begin{bmatrix}0&0&0&0\\0&0&0&0\\0&0&0&0\\w_{t0}'^2\sin\theta_{ji}A_{ji}&0&2w_{t0}'\sin\theta_{ji}A_{ji}&\frac{1}{2}w_{t0}'\sin2\theta_{ji}(S_{\xi ji}+S_{\eta ji})+w_{t0}'\sin\theta_{ji}[(c-\sin\theta_{ji})S_{\xi ji}+(c+\sin\theta_{ji})S_{\eta ji}]\end{bmatrix}\right)\mathrm{d}r\right)\mathbf{q}_{bji}^{e}\right) \tag{21d}$$

$$U_{b5}=\sum_{j=1}^{N}\left(\sum_{i=1}^{N_b}l_{ji}^{e}\mathbf{q}_{bji}^{eT}\left(\int_{-1}^{1}\mathbf{H}_2^{T}\mathbf{H}\otimes\left(-2G_bw_{t0}'^2\cos\theta_{ji}\begin{bmatrix}0&0&0&0\\0&0&0&0\\0&0&0&0\\0&S_{\eta ji}&S_{\xi ji}&cI_{\xi\eta ji}\end{bmatrix}\right)\mathrm{d}r\right)\mathbf{q}_{bji}^{e}\right) \tag{21e}$$

$$U_{b6}=\sum_{j=1}^{N}\left(\frac{1}{2}\sum_{i=1}^{N_b}l_{ji}^{e}q_{bji}^{eT}\Big(\int_{-1}^{1}\mathbf{H}_2^{T}\mathbf{H}_1\otimes\Big(-2E_b\begin{bmatrix}0&S_{\eta ji}&S_{\xi ji}&cI_{\xi\eta ji}\\0&w_{t0}'S_{\eta ji}&w_{t0}'S_{\xi ji}&w_{t0}'cI_{\xi\eta ji}\\0&0&0&0\\0&-w_{t0}'(I_{\xi\eta ji}\cos\theta_{ji}+I_{\eta\eta ji}\sin\theta_{ji})&-w_{t0}'(I_{\xi\xi ji}\cos\theta_{ji}+I_{\xi\eta ji}\sin\theta_{ji})&-w_{t0}'c(I_{\xi\xi\eta ji}\cos\theta_{ji}+I_{\xi\eta\eta ji}\sin\theta_{ji})\end{bmatrix}\right.\right.\right.$$
$$\left.\left.\left.-2w_{t0}'G_b\begin{bmatrix}0&w_{t0}'S_{\eta ji}&w_{t0}'S_{\xi ji}&w_{t0}'cI_{\xi\eta ji}\\0&-S_{\eta ji}&-S_{\xi ji}&-cI_{\xi\eta ji}\\0&S_{\eta ji}&S_{\xi ji}&cI_{\xi\eta ji}\\0&I_{\xi\eta ji}\cos\theta_{ji}+I_{\eta\eta ji}(c+\sin\theta_{ji})&I_{\xi\xi ji}\cos\theta_{ji}+I_{\xi\eta ji}(c+\sin\theta_{ji})&cI_{\xi\xi\eta ji}\cos\theta_{ji}+cI_{\xi\eta\eta ji}(c+\sin\theta_{ji})\end{bmatrix}\Big)\mathrm{d}r\Big)\mathbf{q}_{bji}^{e}\right) \tag{21f}$$

2.5. Tower analytical model

In contrast to other subsystems, the tower has a reasonably simple geometrical shape. The tower is a welded steel shell that is composed of stacked cylindrical and conical shell segments. The loads acting on the tower are contributed by the moments induced by the wind thrust force and the gravitational effect of subsystems the tower support. Also, it may be noted that the direct gravitational force on the tower is very small and is not expected to affect the deformation significantly. Hence, it is omitted to avoid further complications in the system governing equations. The tower has only one global degree-of-freedom w_t to represent its fore-aft movement.

Similar to the rotor discussion above, before proceeding to further derivation, the geometrical properties of the tower cross section are defined as

$$A_t=\pi(D^2-d^2)/4,\quad I_{t\xi\xi}=\pi(D^4-d^4)/64 \tag{22a,b}$$

where D and d are the external and internal diameters of the tower, respectively. These properties will be employed in the subsequent formulation of the tower dynamic model.

From Eq. (1) describing the transformation matrix for the flexible deformation of the thin-walled beam, the displacement of an arbitrary point on the tower neglecting warping effect can be formulated as

$$\mathbf{p}_t=\begin{Bmatrix}\Delta x_t\\ \Delta y_t\\ \Delta z_t\\ 1\end{Bmatrix}=\mathbf{T}_f(0,w_t,0)\cdot\mathbf{T}_{c0}\cdot\{0\ \ \xi_t\ \ \eta_t\ \ 1\}^{T}=\begin{Bmatrix}w_t'\eta_t\\ \xi_t\\ \eta_t\\ 1\end{Bmatrix} \tag{23}$$

where subscript t refer to the tower subsystem. Differentiating the above equation with respect to time t yields the velocity of the point,

$$\dot{\mathbf{p}}_t=\begin{Bmatrix}\eta_t\\ 0\\ 0\\ 0\end{Bmatrix}\dot{w}_t' \tag{24}$$

$$K_t=\int_m\dot{\mathbf{p}}_t^{T}\dot{\mathbf{p}}_t\,\mathrm{d}m=\frac{1}{2}\rho_t\sum_{i=1}^{N_t}\dot{\mathbf{q}}_{ti}^{eT}l_{ti}^{e}\int_{-1}^{1}(\mathbf{H}^{T}\mathbf{H}\otimes I_{t\xi\xi i})\mathrm{d}r\dot{\mathbf{q}}_{ti}^{e} \tag{25}$$

where ρ_t is the material density of the tower, N_t is the number of finite element on the tower and l_t^e is the length of tower finite element.

The potential energy formulation is presented next. From the tower deformation model presented earlier, the derivation of potential energy of tower is reasonably straightforward. First, consider the strain in the tower structure given by

$$\varepsilon_{txx} = \frac{\partial \Delta x_t}{\partial x} = \mathbf{q}_t' \eta_t, \quad \varepsilon_{txz} = \frac{\partial \Delta x_t}{\partial \eta_t} + \frac{\partial \Delta z_t}{\partial x_t} = \mathbf{q}_t \tag{26a,b}$$

From the above strain equations, the potential energy of the tower can be written as

$$U_t = \int_V (E_t \varepsilon_{txx}^{\mathrm{T}} \varepsilon_{txx} + G_t \varepsilon_{txz}^{\mathrm{T}} \varepsilon_{txz})\, \mathrm{d}V = \frac{1}{2} \sum_{i=1}^{N_t} \dot{q}_{ti}^{e\mathrm{T}} l_{ti}^e \int_{-1}^{1} (E_t \mathbf{H}_1^{\mathrm{T}} \mathbf{H}_1 \otimes I_{t\xi\xi i} + G_t H^{\mathrm{T}} H \otimes A_{ti})\, \mathrm{d}r \mathbf{q}_{ti}^e \tag{27}$$

where E_t and G_t are tower and blade shear elastic modulus, respectively.

2.6. Nacelle analytical model

In addition to the kinetic energy terms for the blades and tower, the other parts are also significant sources of kinetic energy including nacelle, hub, shafts, gearbox and generator. Those components are regarded as rigid bodies and their mass effects are integrated into the mass of nacelle. Assuming the total nacelle mass is m_n and center of gravity is C_N=(x_g, 0, z_g), the displacement of the nacelle centroid relative to the inertial coordinate system can be written as

$$\mathbf{p}_n = \mathbf{T}_f(0, w_{t0}, 0) \cdot T_{n0} \cdot \{x_g \;\; 0 \;\; z_g \;\; 1\}^{\mathrm{T}} = \begin{Bmatrix} z_g + H - w_{t0}' x_g \\ 0 \\ -w_{t0}'(z_g + H) - x_g \\ 1 \end{Bmatrix} \tag{28}$$

Differentiating the above equation with respect to time t yields the velocity of the nacelle centroid as

$$\dot{\mathbf{p}}_n = -\dot{w}_{t0}' \begin{Bmatrix} x_g \\ 0 \\ (z_g + H) \\ 0 \end{Bmatrix} \tag{29}$$

Similar to earlier kinetic energy derivations, using the above velocity expression, the kinetic energy contributed by the nacelle housing and all its internal components can be shown to be

$$K_n = \int_m \dot{\mathbf{p}}_n^{\mathrm{T}} \dot{\mathbf{p}}_n\, \mathrm{d}m = m_n \dot{w}_{t0}'^2 [x_g^2 + (z_g + H)^2] \tag{30}$$

2.7. Virtual work of external forces

In the following three sub-sections, the virtual work expressions due to external forces including wind force (aerodynamic loads), centrifugal force and gravity are formulated. The equations for virtual work are needed in the Lagrange method to derive the forcing functions used in the subsequent forced response analysis.

2.7.1. Wind force

The aerodynamic forces exerted on the cross section shown in Fig. 5 can be expressed as

$$\mathrm{d}P = \tfrac{1}{2} \rho_a C_L c_c V_r^2\, \mathrm{d}x_b, \quad \mathrm{d}T = \tfrac{1}{2} \rho_a C_D c_c V_r^2\, \mathrm{d}x_b \tag{31a,b}$$

where dP and dT are the lift and drag forces, respectively, C_L and C_D are the lift and drag coefficients, respectively, c_c is the chord length of the cross section, ρ_a is the air density and V_r is the relative wind velocity given by

$$V_r^2 = V_\infty^2 + (R\omega)^2 \tag{32}$$

where V_∞ is the absolute wind velocity. Note that the aerodynamic force formulation above ignores the effect of pitching moment due to the fact that it is small in magnitude comparing with other aerodynamic components. Since the displacement vector of the center of an arbitrary cross section is

$$\Delta \mathbf{p}_{bc} = \begin{Bmatrix} \Delta x_{bc} \\ \Delta y_{bc} \\ \Delta z_{bc} \end{Bmatrix} = \begin{Bmatrix} u \\ v \\ w \end{Bmatrix} \tag{33}$$

and the aerodynamic force vector acting on the blade is

$$\mathrm{d}\mathbf{F}_a = \{0 \;\; \mathrm{d}P \;\; \mathrm{d}T\}^{\mathrm{T}} \tag{34}$$

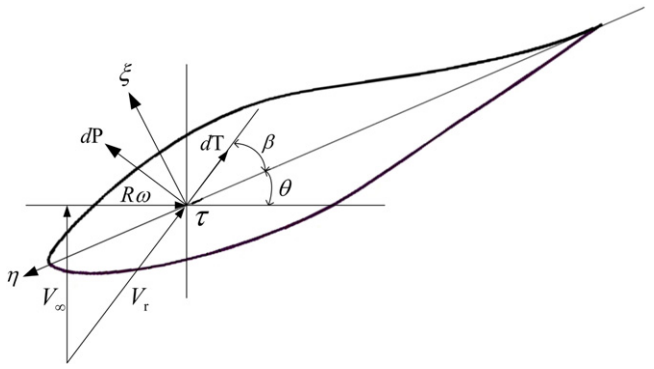

Fig. 5. Distribution of the aerodynamic forces.

the virtual work due to the aerodynamic loads is given by

$$W_a = \int \Delta\mathbf{p}_{bc}^{\mathrm{T}}\,\mathrm{d}\mathbf{F}_a = \frac{1}{2}\rho_a \int c_c V_r^2 \begin{Bmatrix} 0 \\ C_L\sin(\beta+\theta)+C_D\cos(\beta+\theta) \\ -C_L\cos(\beta+\theta)+C_D\sin(\beta+\theta) \\ 0 \end{Bmatrix}^{\mathrm{T}} \mathbf{q}_b\,\mathrm{d}x_b$$

$$= \sum_{j=1}^{N}\left(\frac{1}{4}\rho_a \sum_{i=1}^{N_b} l_{ji}^e c_{cji} V_{rji}^2 \int_{-1}^{1} \mathbf{H}\otimes \begin{Bmatrix} 0 \\ C_{L_{ji}}\sin(\beta_{ji}+\theta_{ji})+C_{D_{ji}}\cos(\beta_{ji}+\theta_{ji}) \\ -C_{L_{ji}}\cos(\beta_{ji}+\theta_{ji})+C_{D_{ji}}\sin(\beta_{ji}+\theta_{ji}) \\ 0 \end{Bmatrix}^{\mathrm{T}} \mathrm{d}r\,\mathbf{q}_{bji}^e\right) \tag{35}$$

It follows that the virtual work of the moment produced by aerodynamic forces on the tower is

$$W_t = \frac{1}{2}\rho_a \int_0^{L_b} c_c V_r^2 [C_L\cos(\beta+\theta) - C_D\sin(\beta+\theta)]\,\mathrm{d}x_b \cdot (H-x_t) w_t'$$

$$= \frac{1}{2}\rho_a \sum_{s=1}^{N_t}\left(\sum_{j=1}^{N}\left\{\sum_{i=1}^{N_b} l_{ji}^e c_{cji} V_{rji}^2 [C_{Lji}\cos(\beta_{ji}+\theta_{ji}) - C_{Dji}\sin(\beta_{ji}+\theta_{ji})]\right\} \cdot \int_{-1}^{1} \mathbf{H}\otimes(H-x_{ts})\mathrm{d}r\,\mathbf{q}_{ts}^e\right) \tag{36}$$

2.7.2. Centrifugal force

It is assumed that the stress caused by the centrifugal force due to the rotation of the blades is distributed uniformly within an arbitrary cross section of the blade. This is a reasonable assumption because all the points on the cross section are about the same distance from the center of blade rotation. Therefore, the virtual work due to centrifugal force can be written as

$$W_c = \int_0^{L_b} u\left(\int_R^{L_b} \rho_b A\,\mathrm{d}s\right) R\omega^2\,\mathrm{d}x_b = \rho_b\omega^2 \sum_{j=1}^{N}\left(\sum_{i=1}^{N_b} \frac{l_{ji}^e}{2}\left(\sum_{s=N_R}^{N_b} A_s l_s^e\right)\right) \int_{-1}^{1} H\otimes[R_{ji}\ \ 0\ \ 0]\,\mathrm{d}r\,\mathbf{q}_{bji}^e \tag{37}$$

At the middle expression, that is the integral included in parenthesis, is the mass of the blade section from R to L_b, s is local coordinates, u is the axial displacement, and L_b is total length of the blade.

2.7.3. Gravity force

Gravity effect can also be a critical factor that needs special attention, especially for large wind turbine structure. Here, the gravity forces on the rotor and the nacelle and its internal components are considered in computing the virtual work due to gravity. The gravity force on the tower is neglected for obvious reasons mentioned earlier. Hence, the virtual work due to gravity can be written as

$$W_g = N\cdot m_b g L w_{t0}' + m_n g x_g w_{t0}' \tag{38}$$

where m_b is a single blade's mass. Next, the system governing equations are derived.

2.8. Governing equations

The Lagrange's equations of motion for the wind turbine system of interest is given by

$$\frac{\mathrm{d}}{\mathrm{d}t}\left(\frac{\partial L_a}{\partial \dot{\mathbf{q}}}\right) - \frac{\partial L_a}{\partial \mathbf{q}} = \mathbf{Q} \tag{39}$$

where $L_a=K_b+K_n+K_t-U_b-U_t$ is the Lagrangian function. Substitution of the Lagrangian into Lagrange's equation above directly yields

$$\frac{\mathrm{d}}{\mathrm{d}t}\frac{\partial(K_b+K_n+K_t)}{\partial\dot{\mathbf{q}}}+\frac{\partial(U_b+U_t)}{\partial\mathbf{q}}=\frac{\partial(W_a+W_t+W_c+W_g)}{\partial\mathbf{q}} \tag{40}$$

Rewriting the above governing equation into a more conventional form

$$\mathbf{M}(w'_{t0})\ddot{\mathbf{q}}+\mathbf{K}\mathbf{q}=\mathbf{Q}(w'_{t0}) \tag{41}$$

where $\mathbf{M}(w'_{t0})$ is the mass matrix and $\mathbf{Q}(w'_{t0})$ is the external force vector acting on the system, which are all a function of the bending slope w'_{t0} of tower most top point. Also, $\mathbf{K}$ is stiffness matrix. The tower displacement vector is $\mathbf{q}_t=\{w'_{t1}\ w'_{t2}\ \cdots\ w'_{t(n_t-1)}\ w'_{t0}\}^{\mathrm{T}}$ and n_t is the node number on the tower. The blade displacement vector is $\mathbf{q}_b=\{\mathbf{q}_{b1}\ \mathbf{q}_{b2}\ \cdots\ \mathbf{q}_{bn_b}\}^{\mathrm{T}}$ and n_b is the node number on the blade having the displacement components given by $\mathbf{q}_{bi}=\{u_i\ v_i\ w_i\ \phi_i\}^{\mathrm{T}}$. The system displacement vector $\mathbf{q}$ is the sum of tower displacement vector $\mathbf{q}_t$ and blade displacement vector $\mathbf{q}_b$, that is $\mathbf{q}=\{\mathbf{q}_t\ \mathbf{q}_{b1}\ \cdots\ \mathbf{q}_{bN}\}^{\mathrm{T}}$. Note that the expressions for $\mathbf{M}(w'_{t0})$, $\mathbf{K}$ and $\mathbf{Q}(w'_{t0})$ are not shown explicitly here since they are too large to be practically included in this paper. Their size is $(148N+61)\times(48N+61)$ for a blade with 37 nodes and 18 elements and the tower with 61 nodes and 30 elements.

3. Numerical example

A horizontal-axis wind turbine system rated at 645 kW is chosen as the numerical example. Its rotor runs upwind of the tower and consists of two NREL S809 blades of length 21.3360 m each. The design parameters of the wind turbine example are presented in Table 1. The geometric parameters and material properties of the discretized blade and tower models constructed from thin-walled finite elements are given in Tables A1 and A2 in Appendix A. The manner in which the lift and drag coefficients of NREL S809 vary with angle of attack is available in Ref. [21].

3.1. Free vibration analysis

In the free vibration analysis, also known as modal analysis, the natural frequencies and mode shapes of the wind turbine system are computed. The natural modes are considered the free response of the system at the corresponding natural frequencies. The problem is setup by letting the external force vector to be zero, that is $\mathbf{Q}(w'_{t0})=\mathbf{0}$, in the system governing equation,

$$\mathbf{M}(w'_{t0})\ddot{\mathbf{q}}+\mathbf{K}\mathbf{q}=\mathbf{0} \tag{42}$$

The above equation is in fact an eigenvalue problem that can be written as

$$\mathbf{K}\boldsymbol{\Phi}=\mathbf{M}(w'_{t0})\boldsymbol{\Phi}\boldsymbol{\Lambda} \tag{43}$$

where the columns in $\boldsymbol{\Phi}$ are the mode shapes and $\boldsymbol{\Lambda}$ is a diagonal matrix of the corresponding natural frequency squares. Since the mass matrix $\mathbf{M}(w'_{t0})$ is a function of tower most top bending slope denoted by w'_{t0}, Eq. (43) can be analyzed given a specific value of w'_{t0}. The results of the dominant natural modes for $w'_{t0}=0$, 0.1, 0.2 are presented in Table 2. Other natural frequencies are not listed explicitly because their contributions to the forced responses are quite small. From the tabulated results, it is obvious that the tower top bending slope w'_{t0} has only a slight influence on the natural frequencies of the tower. This is possibly because only the tower fore-aft bending is represented within the proposed dynamic model.

Table 1
Design parameters used in the wind turbine numerical model.

Parameters	Descriptions	Values
m_n	Mass of the nacelle	23,228 kg
$[x_g\ y_g\ z_g]$	Center of gravity of the nacelle	[0.402 0 0] m
L	Distance from the tower axis to the rotor's rotation plane	3.867 m
H	Longitudinal length of the tower	34.862 m
γ	Blade pitch angle	15°
ω	Rotor angular velocity	26.8 r/min
V_∞	Wind velocity	15 m/s
E_b	Modulus of elasticity of blade	1.7×10^9 Pa
E_t	Modulus of elasticity of tower	2.0×10^{11} Pa
G_b	Shear modulus of blade	7.08×10^9 Pa
G_t	Shear modulus of tower	7.75×10^{10} Pa
ρ_b	Density of blade	2540 kg/m^3
ρ_t	Density of tower	7870 kg/m^3
ρ_b	Density of air	1.293 kg/m^3

Table 2
Dominant natural frequencies and corresponding mode shapes at different tower bending slope.

Natural frequency (Hz)			Mode shape description
$w'_{t0}=0$	$w'_{t0}=0.1$	$w'_{t0}=0.2$	
1.67	1.67	2.16	1st tower bending (with nacelle)
56.32	54.50	45.18	1st rotor anti-symmetrical flap bending
56.54	54.78	45.36	1st rotor symmetrical flap bending
67.31	64.15	58.69	1st rotor anti-symmetrical edge bending
67.34	64.21	58.77	1st rotor symmetrical edge bending
158.72	155.93	149.56	2nd rotor anti-symmetrical flap bending
158.94	156.01	149.87	2nd rotor symmetrical flap bending
190.23	196.17	221.31	2nd rotor anti-symmetrical edge bending
190.56	196.29	221.40	2nd rotor symmetrical edge bending
268.69	294.03	256.44	3rd rotor symmetrical flap bending
724.63	764.24	782.66	2nd tower bending (with nacelle)

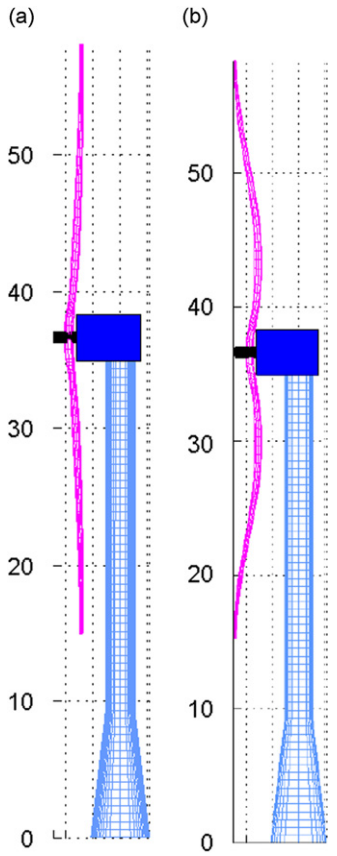

Fig. 6. Rotor's first two symmetrical flap bending mode shapes: (a) 1st flap bending at 56.54 Hz; (b) 2nd flap bending at 158.94 Hz.

Also, the tower bending is strongly coupled with the rotor flap bending but is independent of rotor edge bending. Another interesting observation presented in Table 2 is that first and second tower frequencies are quite far apart. The reason is because they are not just the natural frequencies for the tower structure only, but also the natural frequencies for the combined tower and nacelle. This is due to the fact that the nacelle has no independent degrees of freedom, and its kinetic energy is calculated with respect to the tower's top coordinate w_{t0}. Here, the behavior of the tower is much like that of a vertical hollow beam with a heavy lumped mass at the head. Selected mode shapes of tower, rotor and their coupling are illustrated more clearly in Figs. 6–10. Note that in all subsequent display of analysis results,

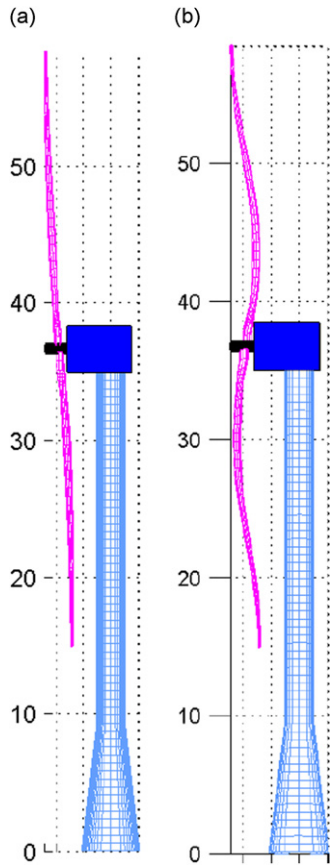

Fig. 7. Rotor's first two anti-symmetrical flap bending mode shapes: (a) 1st flap bending at 56.32 Hz; (b) 2nd flap bending at 158.72 Hz.

rotor is assumed to be in the vertical position even though the formulation does account for the effect of orbital motion of the rotor.

Fig. 6 illustrates the rotor's first two flap bending mode shapes where the two rotor blades deform symmetrically in the same manner. On the other hand, Fig. 7 shows the rotor blades deform in an anti-symmetrically manner. Owing to the fact that the external excitations from the wind effect will be most intense at the low frequency range, these first set of rotor's symmetrical/anti-symmetrical flap mode shapes will have the highest probability of occurrence.

Figs. 8 and 9 illustrate the rotor's first two edge bending mode shapes. In contrast to its flap bending mode shapes, the rotor edge bending mode shapes are uncoupled from the tower deformation because the tower is assumed to possess no motion in the lateral bending direction.

Fig. 10 gives the first two mode shapes of the tower. The tower is composed of stacked cylindrical and conical shell segment with varying inner diameter and thickness. Also, its bottom part has the largest inner diameter and the top contains the thickest shell segment. Hence, the middle part of the tower has the weakest area moment as presented in Table A2 and hence the largest deflection at its second bending mode shape. To make the middle of the tower absorb most potential energy is a sensible design strategy because the root of the tower suffers largest bending moment and the slope of the tower top has a significant effect on the displacement of the blade as it is demonstrated later. Since the cross section material property of the tower is much stiffer than that of the rotor, and the blade modulus of elasticity is only nearly 1 percent of the tower one, it is expected, as shown in these results, that the natural frequencies of the rotor is much lower than that of the tower except for the tower's first natural frequency. Accordingly, at least in this specific design, there is no coupling of mode shapes found between the rotor and tower.

It is also interested to see that the matching pairs of symmetrical and anti-symmetrical rotor natural frequencies are almost the same. For flap bending type modes, the symmetric ones will more likely be excited during operation because the deformations of the blades along the line of the wind path are in phase. On the other hand, for the edge bending type, the anti-symmetric modes will more likely be excited because the deformations of the blades along the tangential direction (related to blade rotation) are in phase. Therefore, in the design of the system, it is probably more important to focus on treating the symmetric flap modes and anti-symmetric edge modes.

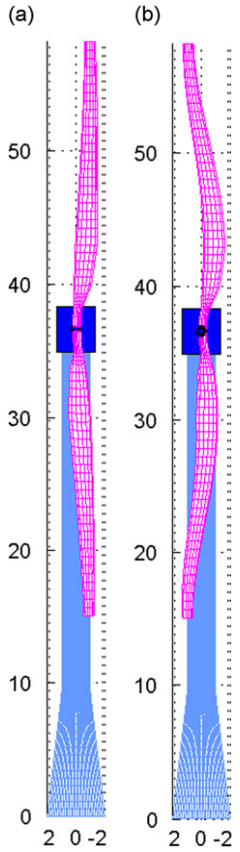

Fig. 8. Rotor's first two symmetrical edge bending mode shapes: (a) 1st edge bending at 67.34 Hz; (b) 2nd edge bending at 190.56 Hz.

3.2. Dynamic stress under constant wind speed

The dynamic stress distributions on the rotor and tower due to wind speed of 15 m/s that corresponds to rotor angular velocity of 26.8 rev/min are analyzed next to demonstrate the capability of forced vibration response model. The proposed governing Eq. (41) is in fact a nonlinear partial differential equation. The nonlinearity is contributed by the non-constant mass matrix $\mathbf{M}(w'_{t0})$and external force vector $\mathbf{Q}(w'_{t0})$ where the variable w'_{t0} is a component of vector $\mathbf{q}$. Therefore, it is impractical to obtain a closed form solution. Here, in analysis, the Newmark numerical integration method is applied. The detailed description of this numerical approach can be found in Refs. [22,23]. The result of applying the proposed numerical method is discussed next.

The dynamic stress expression on the blade and tower can be written, respectively, as

$$\begin{Bmatrix} \boldsymbol{\sigma}_{bxx} \\ \boldsymbol{\tau}_{bxy} \\ \boldsymbol{\tau}_{bxz} \end{Bmatrix} = \begin{bmatrix} E_b & 0 & 0 \\ 0 & G_b & 0 \\ 0 & 0 & G_b \end{bmatrix} \begin{Bmatrix} \varepsilon_{bxx} \\ \varepsilon_{bxy} \\ \varepsilon_{bxz} \end{Bmatrix} = \begin{bmatrix} E_b & 0 & 0 \\ 0 & G_b & 0 \\ 0 & 0 & G_b \end{bmatrix} \left(\begin{Bmatrix} \mathbf{0} \\ \dfrac{\partial \mathbf{S}_{11}}{\partial \xi} \\ \dfrac{\partial \mathbf{S}_{11}}{\partial \eta} \end{Bmatrix} \mathbf{q}_b + \begin{Bmatrix} \mathbf{S}_{11} \\ \dfrac{\partial \mathbf{S}_{21}}{\partial \xi} + \mathbf{S}_{12} \\ \dfrac{\partial \mathbf{S}_{21}}{\partial \eta} + \mathbf{S}_{13} \end{Bmatrix} \mathbf{q}' + \begin{Bmatrix} \mathbf{S}_{21} \\ \mathbf{0} \\ \mathbf{S}_{23} \end{Bmatrix} \mathbf{q}''_b \right) \tag{44}$$

$$\begin{Bmatrix} \boldsymbol{\sigma}_{txx} \\ \boldsymbol{\tau}_{txy} \\ \boldsymbol{\tau}_{txz} \end{Bmatrix} = \begin{bmatrix} E_t & 0 & 0 \\ 0 & G_t & 0 \\ 0 & 0 & G_t \end{bmatrix} \begin{Bmatrix} \varepsilon_{txx} \\ 0 \\ \varepsilon_{txz} \end{Bmatrix} = \begin{bmatrix} E_t & 0 & 0 \\ 0 & G_t & 0 \\ 0 & 0 & G_t \end{bmatrix} \left(\begin{Bmatrix} \mathbf{0} \\ \mathbf{0} \\ \mathbf{1} \end{Bmatrix} \mathbf{q}_t + \begin{Bmatrix} \boldsymbol{\eta}_t \\ \mathbf{0} \\ \mathbf{0} \end{Bmatrix} \mathbf{q}'_t \right) \tag{45}$$

In the above pair of equations, once the dynamic response of the wind turbine structure is computed, the results can be used to compute the dynamic stress distributions. The results when the blades vertically oriented are discussed next.

Fig. 11 shows the distribution of the rotor axial stress $\boldsymbol{\sigma}_{bxx}$ and the tower axial stress $\boldsymbol{\sigma}_{txx}$. As expected, the axial stress increases gradually from the blade tip to its root and reaches its highest value at the root of the blade since it is mainly subjected to the centrifugal force and bending excitation. To illustrate the deformation state of the tower more clearly, the

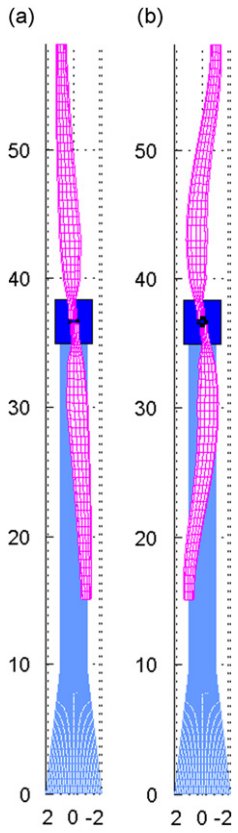

Fig. 9. Rotor's first two anti-symmetrical edge bending mode shapes: (a) 1st edge bending at 67.31 Hz; (b) 2nd edge bending at 190.23 Hz.

displacement of the tower is exaggerated 100 times. The bending of the tower, acting like a giant vertical cantilever beam, is principally caused by the thrust force from the rotor. Thus, it is obvious that the tower front half section endures traction tension, while the tower rear half section experiences pressure tension (not shown). Also, the lower the tower, the higher the tension.

Fig. 12 illustrates the distribution of the rotor shear stress τ_{bxy}. Since the tower is assumed to possess no flexibility in the y-axis direction, the tower shear stress τ_{txy} does not exist. Furthermore, the rotating blade acts like a clamped beam with a distributed force along the axial direction due to the impact from the wind. As a result, the blade experiences the highest shear force at the root, which leads to the maximum shear stress τ_{bxy} at the same location.

Fig. 13 presents the distributions of the rotor shear τ_{bxz} and the tower shear stress τ_{txz}. The shear stress τ_{bxz} has a similar distribution as the shear stress τ_{bxy} for the same reason described above. The tower shear stress τ_{txz} is the same at the circumference of a cross section of the tower and varies with the latitude of the tower. The least shear stress occurs at the root of the tower where the cross sectional area is greatest.

3.3. Coupled blade–tower dynamic response

The forced response analysis shows that the tower property has a significant influence on the dynamical behavior of the rotor. One can observed from Eq. (16) that the displacement of a point on the rotor is amplified because of the bending deformation of the tower. Fig. 14 shows the comparison of the influence of the tower stiffness on the rotor tip dynamic displacement. The change of the tower's physical property is listed in Table 3. Tower I is a typical one with varying diameter and thickness, tower II is similar to tower I but with an average skin thickness 0.0182 m, and tower III possesses only 80 percent of the diameters of that of tower II. Within Fig. 14, solid line is used for tower I, dashed line for tower II and dotted line for tower III responses. It is clear that the dynamical performance of towers I and II have no fundamental difference when comparing the rotor tip displacement. However, tower I saves around 5 percent materials. When the diameter of tower III reduces to 80 percent to that of tower II, the dynamic displacements of the rotor tip are nearly doubled.

Also observed in Fig. 14, due to the deformation coupling between the blade and tower, the blade's tip dynamic displacements in the vertical and fore-aft directions vary temporarily in a very similar way. Their primary vibration

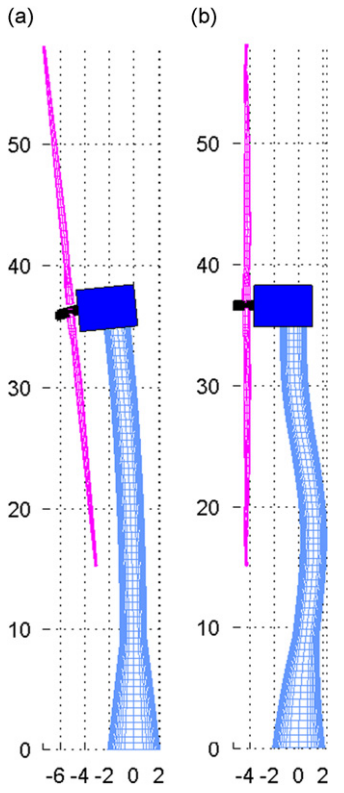

Fig. 10. Tower's first two bending mode shapes: (a) 1st bending at 1.67 Hz; (b) 2nd bending at 724.63 Hz.

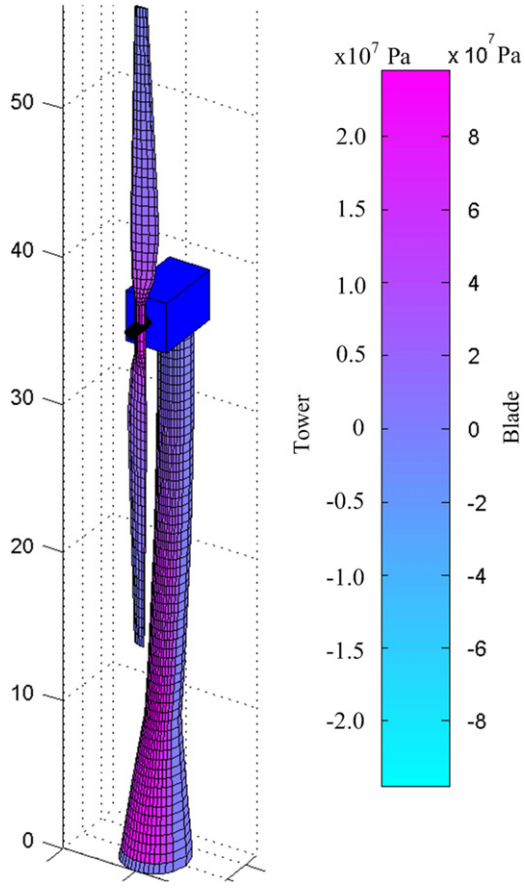

Fig. 11. Distributions of the rotor axial stress σ_{bxx} and the tower axial stress σ_{txx}.

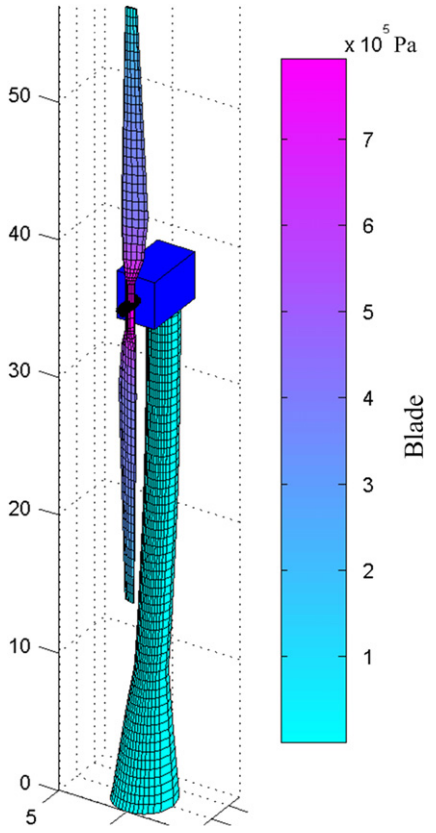

Fig. 12. Distributions of the rotor shear stress τ_{bxy}.

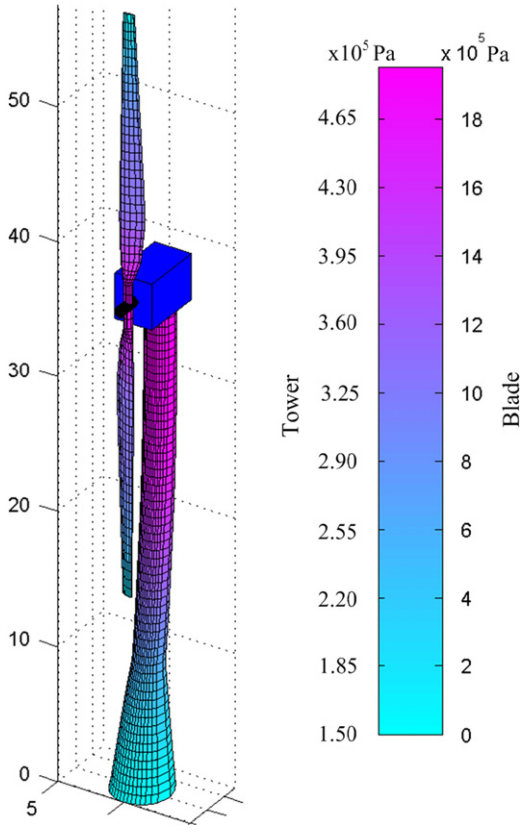

Fig. 13. Distributions of the rotor shear stress τ_{bxz} and tower shear stress τ_{txz}.

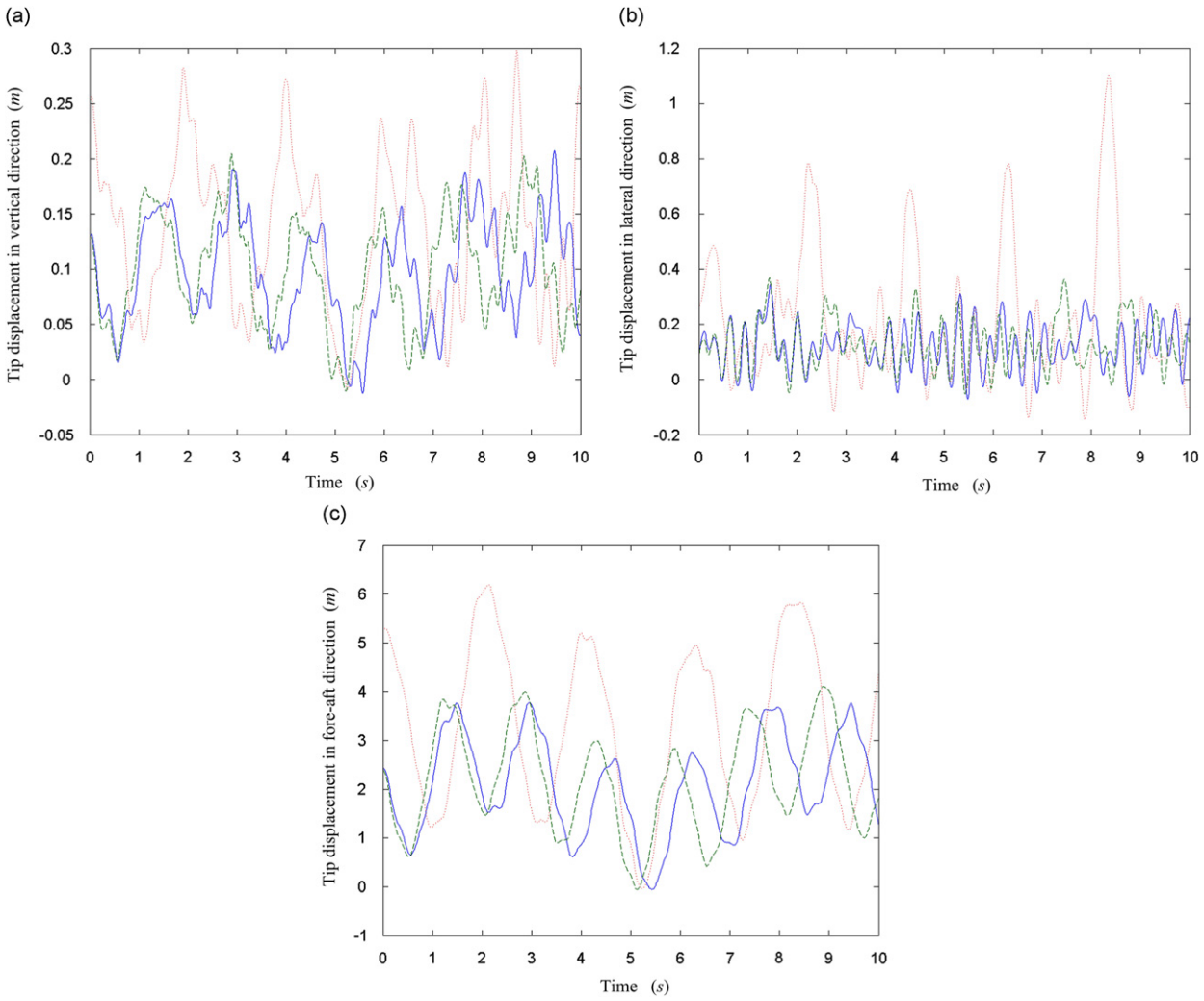

Fig. 14. The blade tip displacement of tower I (solid line), tower II (dashed line) and tower III (dotted line). (a) Blade tip displacement along vertical direction; (b) blade tip displacement along lateral direction; (c) blade tip displacement along fore-aft direction.

Table 3
Design parameters for towers I, II and III.

x (m)	Tower I		Tower II		Tower III	
	Diameter (m)	Thickness (m)	Diameter (m)	Thickness (m)	Diameter (m)	Thickness (m)
0.000	4.267	0.0142	4.267	0.0182	3.4136	0.0182
2.294	3.734	0.0142	3.734	0.0182	2.9872	0.0182
6.867	2.692	0.0207	2.692	0.0182	2.1536	0.0182
9.145	2.134	0.0239	2.134	0.0182	1.7072	0.0182
11.481	2.134	0.0239	2.134	0.0182	1.7072	0.0182
14.986	2.134	0.0239	2.134	0.0182	1.7072	0.0182
17.909	2.134	0.0157	2.134	0.0182	1.7072	0.0182
21.417	2.134	0.0157	2.134	0.0182	1.7072	0.0182
24.339	2.134	0.0157	2.134	0.0182	1.7072	0.0182
27.248	2.134	0.0104	2.134	0.0182	1.7072	0.0182
30.727	2.134	0.0104	2.134	0.0182	1.7072	0.0182
33.664	2.134	0.0239	2.134	0.0182	1.7072	0.0182
34.862	2.134	0.0239	2.134	0.0182	1.7072	0.0182

frequency is about 0.167 Hz that corresponds exactly to the natural frequency of the first tower bending mode. This result clearly demonstrates that the tower's deformation has considerable impact on the blade's dynamic displacement. Hence, it is desirable that the tower structure is designed with sufficient strength and rigidity.

4. Conclusions

This study proposes a mixed flexible-rigid multi-body dynamic model to predict the deformation state and dynamic stress distributions of a wind turbine system. The proposed formulation possesses the following features and enhancements over previous models.

(1) The proposed analytical model employs the thin-walled beam theory that is superior to the traditional 1-D beam finite element when applied to compute the dynamic behavior of wind turbine. This is because the proposed formulation can, not only provide significant amount of detailed response information on the flexible part of the system, namely the blade and tower structures, but also inherits the simplicity of the 1-D beam finite element modeling concept.
(2) Due to the combination of centrifugal force and aerodynamic force, the blade's maximum stress occurs at the root. The tower is mainly subjected to the thrust force from the rotor and acts like a clamped cantilever beam. The fact that both blade and tower are typical slender structure makes the dynamical behavior of the wind turbine system depicts significant first-order mode shape character.
(3) The stiffness of the tower structure has a significant impact on the dynamical behavior of overall wind turbine system. The flexibility of the tower accentuates the dynamic displacement of the blade greatly. That is one of the reasons modern wind turbine must be designed with strong and rigid tower. However, to minimize the use of extraneous materials, tower with varying cross section should be used.

Acknowledgments

The authors would like to acknowledge the support and contributions from the State Key Lab of Mechanical Transmission, Chongqing University, China. The research is also funded by the National Natural Science Foundation of China (Contract no. 50675231).

Appendix A

The geometric parameters and material properties of the discretized blade and tower models constructed from thin-walled finite elements are given in Tables A1 and A2, respectively.

Table A1
Physical properties of the blade.

Node number	x_b (m)	Twist α (deg)	Chord c_c (m)	$A\times10^{-1}$ (m^2)	$S_y\times10^{-2}$ (m^3)	$I_{yy}\times10^{-2}$ (m^4)	$I_{zz}\times10^{-2}$ (m^4)	$I_{yz}\times10^{-4}$ (m^4)	$I_{yyz}\times10^{-4}$ (m^5)	$I_{yzz}\times10^{-4}$ (m^5)	$I_{yyy}\times10^{-2}$ (m^5)	$I_{zzz}\times10^{-6}$ (m^5)
1	0	0		0.88	0	1.18	1.18	0	0	−5.45	−0.16	0
2	0.6905	0		2.19	−1.11	2.30	1.32	0	0	−5.45	−0.16	0
3	1.3810	0	0.6	2.90	−2.62	3.32	1.39	0	0	−5.45	−0.16	0
4	1.6050	3.42	1.171	2.99	−3.07	3.56	1.38	−1.77	1.27	−1.09	−1.07	−1.25
5	1.8290	3.37	1.196	2.99	−3.47	3.74	1.35	−1.89	1.38	−1.18	−1.16	−1.36
6	2.1335	3.31	1.231	2.88	−3.90	3.85	1.29	−2.06	1.55	−1.33	−1.31	−1.52
7	2.4380	3.27	1.268	2.69	−4.19	3.71	1.19	−2.25	1.75	−1.50	−1.47	−1.71
8	3.0475	3.18	1.341	2.30	−4.54	3.61	1.00	−2.67	2.16	−1.87	−1.84	−2.14
9	3.6570	3.08	1.411	2.03	−4.83	3.76	0.83	−3.11	2.68	−2.29	−2.26	−2.62
10	4.2670	2.98	1.478	1.92	−5.33	4.00	0.73	−3.57	3.23	−2.77	−2.72	−3.16
11	4.8770	2.88	1.555	1.89	−5.93	4.12	0.66	−4.16	3.95	−3.38	−3.33	−3.87
12	5.4865	2.79	1.643	1.82	−6.41	4.02	0.58	−4.90	4.92	−4.22	−4.15	−4.82
13	6.0960	2.69	1.699	1.72	−6.53	3.67	0.50	−5.42	5.63	−4.82	−4.74	−5.51
14	6.7310	2.57	1.685	1.62	−6.14	3.27	0.43	−5.29	5.44	−4.66	−4.58	−5.33
15	7.3660	2.45	1.637	1.52	−5.64	3.03	0.38	−4.85	4.85	−4.16	−4.08	−4.75
16	8.0010	2.33	1.603	1.45	−5.43	2.79	0.33	−4.55	4.46	−3.82	−3.76	−4.37
17	8.6360	2.21	1.575	1.37	−5.18	2.38	0.29	−4.32	4.16	−3.56	−3.50	−4.07
18	9.2710	2.06	1.537	1.26	−4.56	1.98	0.25	−4.02	3.77	−3.23	−3.18	−3.70
19	9.9060	1.91	1.493	1.15	−3.93	1.77	0.21	−3.69	3.37	−2.88	−2.83	−3.30
20	10.541	1.77	1.452	1.08	−3.65	1.77	0.18	−3.39	3.01	−2.57	−2.53	−2.95
21	11.176	1.61	1.412	1.02	−3.44	1.62	0.15	−3.11	2.69	−2.30	−2.26	−2.63

Table A1 (*continued*)

Node number	x_b (m)	Twist α (deg)	Chord c_c (m)	$A\times10^{-1}$ (m^2)	$S_y\times10^{-2}$ (m^3)	$I_{yy}\times10^{-2}$ (m^4)	$I_{zz}\times10^{-2}$ (m^4)	$I_{yz}\times10^{-4}$ (m^4)	$I_{yyz}\times10^{-4}$ (m^5)	$I_{yzz}\times10^{-4}$ (m^5)	$I_{yyy}\times10^{-2}$ (m^5)	$I_{zzz}\times10^{-6}$ (m^5)
22	11.811	1.43	1.372	0.93	−3.00	1.36	0.13	−2.85	2.39	−2.05	−2.01	−2.34
23	12.446	1.24	1.331	0.84	−2.53	1.11	0.10	−2.61	2.12	−1.82	−1.79	−2.08
24	13.081	1.06	1.291	0.77	−2.29	0.96	0.08	−2.37	1.87	−1.61	−1.58	−1.84
25	13.716	0.86	1.250	0.71	−2.11	0.85	0.07	−2.16	1.65	−1.41	−1.39	−1.61
26	14.351	0.63	1.209	0.64	−1.80	0.70	0.05	−1.95	1.44	−1.24	−1.22	−1.45
27	14.986	0.38	1.168	0.56	−1.49	0.55	0.04	−1.76	1.26	−1.08	−1.06	−1.23
28	15.621	0.15	1.127	0.51	−1.31	0.45	0.03	−1.58	1.09	−0.93	−0.92	−1.07
29	16.256	−0.11	1.087	0.46	−1.17	0.38	0.03	−1.42	0.94	−0.81	−0.79	−0.92
30	16.891	−0.43	1.047	0.40	−0.97	0.30	0.02	−1.27	0.81	−0.69	−0.68	−0.79
31	17.526	−0.77	1.006	0.34	−0.78	0.22	0.01	−1.13	0.69	−0.59	−0.58	−0.68
32	18.161	−1.08	0.966	0.30	−0.66	0.18	0.01	−1.00	0.59	−0.50	−0.49	−0.58
33	18.796	−1.43	0.925	0.27	−0.58	0.15	0.01	−0.86	0.49	−0.42	−0.42	−0.49
34	19.431	−1.87	0.884	0.25	−0.50	0.13	0.01	−0.76	0.41	−0.35	−0.35	−0.40
35	20.066	−2.37	0.843	0.23	−0.43	0.10	0.00	−0.66	0.34	−0.29	−0.29	−0.33
36	20.701	−2.87	0.802	0.22	−0.38	0.09	0.00	−0.57	0.28	−0.24	−0.24	−0.27
37	21.336	−3.31	0.762	0.21	−0.36	0.08	0.00	−0.49	0.23	−0.20	−0.19	−0.22

Table A2
Physical properties of the tower.

Node number	x_t (m)	d (m)	D (m)	A_t (m^2)	I_{yyt} (m^4)	Node number	x_t (m)	d (m)	D (m)	A_t (m^2)	I_{yyt} (m^4)
1	0.00	4.267	4.295	0.191	0.437	31	17.43	2.134	2.168	0.115	0.066
2	0.58	4.132	4.160	0.185	0.395	32	18.01	2.134	2.165	0.106	0.061
3	1.16	3.997	4.025	0.178	0.359	33	18.59	2.134	2.165	0.106	0.061
4	1.74	3.862	3.890	0.172	0.324	34	19.17	2.134	2.165	0.106	0.061
5	2.32	3.727	3.755	0.164	0.292	35	19.75	2.134	2.165	0.106	0.061
6	2.90	3.594	3.625	0.170	0.278	36	20.33	2.134	2.165	0.106	0.061
7	3.48	3.462	3.494	0.173	0.262	37	20.91	2.134	2.165	0.106	0.061
8	4.06	3.330	3.363	0.175	0.246	38	21.49	2.134	2.165	0.106	0.061
9	4.64	3.196	3.232	0.177	0.229	39	22.07	2.134	2.165	0.106	0.061
10	5.22	3.065	3.102	0.178	0.211	40	22.66	2.134	2.165	0.106	0.061
11	5.81	2.932	2.971	0.178	0.193	41	23.24	2.134	2.165	0.106	0.061
12	6.39	2.800	2.840	0.177	0.176	42	23.82	2.134	2.165	0.106	0.061
13	6.97	2.666	2.708	0.176	0.158	43	24.40	2.134	2.165	0.106	0.060
14	7.55	2.523	2.567	0.173	0.140	44	24.98	2.134	2.163	0.105	0.056
15	8.13	2.381	2.462	0.169	0.122	45	25.56	2.134	2.161	0.098	0.052
16	8.71	2.239	2.285	0.165	0.106	46	26.14	2.134	2.159	0.090	0.048
17	9.29	2.134	2.182	0.162	0.094	47	26.72	2.134	2.157	0.083	0.044
18	9.87	2.134	2.182	0.162	0.094	48	27.30	2.134	2.155	0.076	0.040
19	10.45	2.134	2.182	0.162	0.094	49	27.88	2.134	2.155	0.070	0.040
20	11.03	2.134	2.182	0.162	0.094	50	28.47	2.134	2.155	0.070	0.040
21	11.62	2.134	2.182	0.162	0.094	51	29.05	2.134	2.155	0.070	0.040
22	12.20	2.134	2.182	0.162	0.094	52	29.63	2.134	2.155	0.070	0.040
23	12.78	2.134	2.182	0.162	0.094	53	30.21	2.134	2.155	0.070	0.040
24	13.36	2.134	2.182	0.162	0.094	54	30.79	2.134	2.155	0.072	0.041
25	13.94	2.134	2.182	0.162	0.094	55	31.37	2.134	2.161	0.090	0.052
26	14.52	2.134	2.182	0.162	0.094	56	31.95	2.134	2.166	0.108	0.062
27	15.10	2.134	2.181	0.159	0.093	57	32.53	2.134	2.171	0.126	0.073
28	15.68	2.134	2.178	0.148	0.086	58	33.11	2.134	2.177	0.144	0.084
29	16.26	2.134	2.175	0.137	0.079	59	33.69	2.134	2.182	0.162	0.094
30	16.85	2.134	2.171	0.126	0.073	60	34.28	2.134	2.182	0.162	0.094
						61	34.86	2.134	2.182	0.162	0.094

References

[1] D.C. Quarton, The evolution of wind turbine design analysis—a twenty year progress review, *Wind Energy* 1 (1998) 5–24.
[2] A. Baumgart, A mathematical model for wind turbine blades, *Journal of Sound and Vibration* 251 (1) (2002) 1–12.
[3] R. Younsi, I. El-Batanony, J. Tritsch, H. Naji, B. Landjerit, Dynamic study of wind turbine blade with horizontal axis, *European Journal of Mechanics—A/Solids* 20 (2001) 241–252.
[4] P.J. Murtagh, B. Basu, B.M. Broderick, Mode acceleration approach for rotating wind turbine blades, *Proceedings of the Institution of Mechanical Engineers. Part K: Journal of Multi-body Dynamics* 218 (3) (2004) 159–166.

[5] P.K. Chaviaropoulos, I.G. Nikolaou, K.A. Aggelis, et al., Viscous and aeroelastic effects on wind turbine blades. The VISCEL Project. Part I: 3D Navier–Stokes rotor simulations, *Wind Energy* 6 (2003) 365–385.
[6] C. Kong, J. Bang, Y. Sugiyama, Structural investigation of composite wind turbine blade considering various load cases and fatigue life, *Energy* 30 (2005) 2101–2114.
[7] J. Wang, D. Qin, Q. Zhang, Mathematical model for predicting the blade behaviour of horizontal axis wind turbine, *Proceedings of IMechE. Part C: Journal of Mechanical Engineering Science* 222 (2008) 1681–1694.
[8] H.M. Negm, K.Y. Maalawi, Structural design optimization of wind turbine towers, *Computers and Structures* 74 (2000) 649–666.
[9] I. Lavassas, G. Nikolaidis, P. Zervas, E. Efthimiou, I.N. Doudoumis, C.C. Baniotopoulos, Analysis and design of the prototype of a steel 1-MW wind turbine tower, *Engineering Structures* 25 (2003) 1097–1106.
[10] N. Bazeos, G.D. Hatzigeorgiou, I.D. Hondros, H. Karamaneas, D.L. Karabalis, D.E. Beskos, Static, seismic and stability analyses of a prototype wind turbine steel tower, *Engineering Structures* 24 (2002) 1015–1025.
[11] P.J. Murtagh, B. Basu, B.M. Broderick, Along-wind response of a wind turbine tower with blade coupling subjected to rotationally sampled wind loading, *Engineering Structures* 27 (2005) 1209–1219.
[12] A.D. Garrad, D.C. Quarton, Symbolic computing as a tool in wind turbine dynamics, *Journal of Sound and Vibration* 109 (1) (1986) 65–78.
[13] K. Stol, M. Balas, G. Bir, Floquet modal analysis of a teetered—Rotor wind turbine, *ASME Journal of Solar Energy Engineering* 124 (2002) 364–371.
[14] J.W. Larsen, S.R.K. Nilsen, Nonlinear parameteric instability of wind turbine wings, *Journal of Sound and Vibration* 299 (2007) 64–82.
[15] A. Ahlstrom, Influence of wind turbine flexibility on loads and power production, *Wind Energy* 9 (3) (2005) 237–249.
[16] D. Lee, D.H. Hodges, M.J. Patil, Multi-flexible-body dynamic analysis of horizontal axis wind turbines, *Wind Energy* 5 (2002) 281–300.
[17] D. Lee, D.H. Hodges, Multi-flexible-body analysis for application to wind turbine control design, NREL/SR-500-35228, 2004.
[18] A.H. Nayfeh, P.F. Pai, *Linear and Nonlinear Structural Mechanics*, John Wiley & Sons Inc., Hoboken, NJ, 2004.
[19] D.H. Hodges, E.H. Dowell, Nonlinear equations of motion for the elastic bending and torsion of twisted non-uniform rotor blades, NASA TN-7818, 1974.
[20] H. Sush, C.W. Radcliffe, *Kinematics and Mechanisms Design*, John Wiley & Sons Inc., Hoboken, NJ, 1978.
[21] D.A. Griffin, NREL advanced research turbine (ART) aerodynamic design of ART-2B rotor blades, NREL/SR-500-28473, August 2000.
[22] K.J. Bathe, *Finite Element Procedures in Engineering Analysis*, Prentice-Hall, Englewood Cliffs, 1982.
[23] J.G. Jalon, E. Bayo, *Kinematic and Dynamic Simulation of Multibody Systems*, Springer-Verlag, New York, 1994.